Rigorous symmetry adaptation of multiorbital rotationally invariant slave-boson theory with application to Hund's rules physics

Christoph Piefke and Frank Lechermann
I. Institut für Theoretische Physik, Universität Hamburg, D-20355 Hamburg, Germany

(Received 24 October 2017; revised manuscript received 20 March 2018; published 30 March 2018)

The theory of correlated electron systems on a lattice proves notoriously complicated because of the exponential growth of Hilbert space. Mean-field approaches provide valuable insight when the self-energy has a dominant local structure. Additionally, the extraction of effective low-energy theories from the generalized many-body representation is highly desirable. In this respect, the rotational-invariant slave-boson (RISB) approach in its mean-field formulation enables versatile access to correlated lattice problems. However, in its original form, due to numerical complexity, the RISB approach is limited to about three correlated orbitals per lattice site. We thus present a thorough symmetry-adapted advancement of RISB theory, suited to efficiently deal with multiorbital Hubbard Hamiltonians for complete atomic-shell manifolds. It is utilized to study the intriguing problem of Hund's physics for three- and especially five-orbital manifolds on the correlated lattice, including crystal-field terms as well as spin-orbit interaction. The well-known Janus-face phenomenology, i.e., strengthening of correlations at smaller-to-intermediate Hubbard U accompanied by a shift of the Mott transition to a larger U value, has a stronger signature and more involved multiplet resolution for five-orbital problems. Spin-orbit interaction effectively reduces the critical local interaction strength and weakens the Janus-face behavior. Application to the realistic challenge of Fe chalcogenides underlines the subtle interplay of the orbital degrees of freedom in these materials.

DOI: 10.1103/PhysRevB.97.125154

I. INTRODUCTION

The dichotomy of higher-energy localization and lower-energy itinerancy poses a key challenge of correlated electron systems on lattices with spatial dimension dim >1. To cope with this problem on general grounds, many-body theory has to cover a large energy window, rendering standard perturbation theory or renormalization-group approaches difficult. Integrating out degrees of freedom is notoriously complex. Only if the physics singles out a certain energy scale, e.g., low energy in the Kondo problem, (numerical) exact theoretical methods become available.

Auxiliary-particle or Gutzwiller-based [1] schemes approach the given problem in a simplified, but often qualitatively adequate way, that is especially useful to study low-temperature properties of correlated electron systems in the thermodynamic limit. Instead of aiming for a complete treatment of the lattice electrons' dichotomy with further necessary approximations in real or reciprocal space, temperature or frequency range, key focus is on an approximate handling of the two-faced character of the electrons. A certain protocol for liberating the itinerant from the localized degrees of freedom is common to all the various flavors of these schemes. In this work, we concentrate on the auxiliary- or "slave" -particle methods, but in practice the Gutzwiller frameworks carry in principle the same physics [2], using a different representation/language [3–5].

Originally introduced [6] to handle the Anderson model, the slave-boson concept was further developed in the context of mixed-valent and Kondo-lattice systems [7,8], and afterwards has been modified and extended in various directions over the years [9–20]. The main idea is to distinguish between the localized and the delocalized character of an electron on the operator level. In its simplest one-orbital form at infinite local interaction strength U, one introduces a quasiparticle (QP) fermionic operator f for the itinerant behavior, while a bosonic operator ϕ takes care of the strictly local empty state on lattice site i. Therewith, the physical electron creation operator $c^\dagger$ may be reexpressed, and a straightforward constraint to abandon doubly occupied lattice sites established, i.e.,

$$c^\dagger_{i\sigma} = f^\dagger_{i\sigma}\phi_i \quad \wedge \quad \sum_{i\sigma} f^\dagger_{i\sigma} f_{i\sigma} + \phi^\dagger_i \phi_i = 1, \qquad (1)$$

whereby $\sigma = \uparrow,\downarrow$ marks the spin projection. This efficient route to select the physical states on an interacting lattice can be generalized by various means. Kotliar and Ruckenstein [9] increased the number of local bosons to describe finite-U cases. Multiorbital extensions thereof ask for a further increase of the bosonic variables [14]. In parallel, there are options to replace/modify the character of the auxiliary particle in order to strengthen or focus on certain aspects of the correlated electron problem. For instance, the slave-rotor method [15] and the slave-spin framework [16] are two such alternative theories.

This work deals with an efficient realization of the rotational-invariant slave-boson (RISB) theory [12,17,18], an elaborate generalization of the original ideas for manifest multiorbital problems. Rotational invariance in the theoretical description is essential to promote the simple one-orbital empty-state bosonic degree of freedom to an object that can address the intricate multiplet structure of a local quantum-chemical entity in full generality, *as well as* its general coupling to the k-dependent quasiparticle degrees of freedom. The RISB framework handles these issues properly and it has been successfully utilized to study various correlated condensed matter problems, both on the model level and using realistic dispersions in the context of concrete materials. Namely, applications to multiorbital Mott transitions [17,21], quasi-two-dimensional lattices [22–25], spin-orbit and related anisotropic interactions [26–28], three-orbital Hund's physics [21,29], multiorbital superconductivity [18], and real-space defect problems [30] were performed. In addition, inspired by a Gutzwiller-based scheme [31], a time-dependent extension to address nonequilibrium electronic correlations has also been put forward [29,32,33].

However, the number of auxiliary bosons grows exponentially with the number of orbitals, as expected for a method coping with a faithful coverage of the generic quantum Hilbert space. Therefore, we here report an advancement of the RISB framework that makes rigorous use of the various detailed symmetries of the lattice problem at hand. This allows us to perform full transition-metal d-shell investigations with general Coulomb interactions and including crystal fields and spin-orbit coupling. Moreover, the methodology may be combined with density functional theory (DFT) in a charge self-consistent manner. We apply the generalized scheme to study the prominent Hund's physics [34–37] in three- and five-orbital model Hamiltonians and provide results within the materials context of FeSe and FeTe.

The paper is organized as follows. In Sec. II the basic principles of RISB are introduced for the canonical single-band case, in line with a brief classification of the formalism in view of other many-body techniques. Section III discusses the characteristics of the available multiorbital model Hamiltonians. The technical Sec. IV presents the symmetry-adapted RISB extension to many orbitals. A compendious account of combining RISB with DFT to approach realistic systems is given in Sec. V. Finally, Sec. VI deals with the selected applications to model and materials problems in the broader context of Hund's physics.

II. BRIEF SURVEY OF ROTATIONAL-INVARIANT SLAVE-BOSON THEORY

To set the stage, we first provide a short overview about the key methodological steps of the RISB approach on the basis of the canonical single-band Hubbard model. This serves the goal to introduce the principles of the theory, which is generalized to the symmetry-adapted multiorbital case in Sec. IV. Additionally, this then allows us to discuss the important mean-field (or saddle-point) approximation as well as comparisons to other many-body schemes. For a general, more detailed introduction to RISB, see Ref. [17].

A. Single-orbital formalism

The Hamiltonian for the single-band Hubbard model with nearest-neighbor hopping t and local Coulomb repulsion U reads as [38]

$$\mathcal{H} = -t \sum_{ij\sigma} c^\dagger_{i\sigma} c_{j\sigma} + U \sum_i n_{i\uparrow} n_{i\downarrow} \equiv \mathcal{H}^{(\mathrm{kin})} + \sum_i \mathcal{H}_i^{(\mathrm{loc})}, \tag{2}$$

with i,j labeling lattice sites. For the following, the details of the crystal lattice are irrelevant, and we assume a Bravais lattice in spatial dimension $\dim > 1$ [39].

On a lattice site i, the four possible electron states are given by

$$\mathcal{A} = \{|E\rangle, |S_\downarrow\rangle, |S_\uparrow\rangle, |D\rangle\}, \tag{3}$$

i.e., an empty site $|E\rangle$, a site $|S_\sigma\rangle$ occupied by a single electron with spin projection σ, and a site $|D\rangle$ occupied by two electrons of opposite spin are represented in RISB in full generality through acting on the vacuum state $|\mathrm{vac}\rangle$ as follows:

$$|E\rangle = |0\rangle = \phi_E^\dagger\,|\mathrm{vac}\rangle, \tag{4}$$

$$|S_\downarrow\rangle = |{\downarrow}\rangle = \tfrac{1}{2}\{\phi^\dagger_{\downarrow\uparrow}\, f^\dagger_\uparrow + \phi_{\downarrow\downarrow}\, f^\dagger_\downarrow\}\,|\mathrm{vac}\rangle, \tag{5}$$

$$|S_\uparrow\rangle = |{\uparrow}\rangle = \tfrac{1}{2}\{\phi^\dagger_{\uparrow\uparrow}\, f^\dagger_\uparrow + \phi_{\uparrow\downarrow}\, f^\dagger_\downarrow\}\,|\mathrm{vac}\rangle, \tag{6}$$

$$|D\rangle = |{\uparrow\downarrow}\rangle = \phi_D^\dagger\,|\mathrm{vac}\rangle. \tag{7}$$

Thus, the method introduces two fermionic QP operators and six bosonic operators on every site, i.e.,

$$\text{site } i: \quad f_\downarrow, f_\uparrow, \phi_E, \begin{pmatrix} \phi_{\downarrow\downarrow} & \phi_{\uparrow\downarrow} \\ \phi_{\downarrow\uparrow} & \phi_{\uparrow\uparrow} \end{pmatrix}, \phi_D. \tag{8}$$

The second index on the single-particle bosons refers to a QP degree of freedom, whereas the first index is generally associated with the local state. The physics of this higher-dimensional bosonic-operator structure may be read off from Eqs. (5) and (6). A low-energy QP excitation is not necessarily only connected to its spin-*identical* high-energy local counterpart, but may also connect to other local configurations: in this simple case, a state with opposite spin configuration. This general structure renders it possible to account for full rotational invariance in the description.

Choosing these four slave-boson operators in the one-particle sector, derived by physical intuition, already accounts for a given symmetry of the system: particle-number symmetry is included, there exists no slave-boson operator that mixes two states with different number of particles. In fact, since we aim for a matrix-based formulation, these four objects can be organized in a larger slave-boson operator matrix on the set $\mathcal{A}$, i.e.,

$$\Phi = \begin{array}{c} \\ \\ \end{array}\begin{array}{ccccc} & E & S_\downarrow & S_\uparrow & D \\ E & \phi_E & 0 & 0 & 0 \\ S_\downarrow & 0 & \phi_{\downarrow\downarrow} & \phi_{\uparrow\downarrow} & 0 \\ S_\uparrow & 0 & \phi_{\downarrow\uparrow} & \phi_{\uparrow\uparrow} & 0 \\ D & 0 & 0 & 0 & \phi_D \end{array}. \tag{9}$$

Note that the matrix Φ is block diagonal in particle numbers with (as color coded) zero-particle sector 🟥 one-particle sector 🟦, and two-particle sector 🟩. Its matrix elements ϕ_{AB} with $A,B \in \mathcal{A}$ are labeled by all available local states. Already here, be aware that throughout this work, we exclude the possibility for pairing instabilities and therefore do not couple different particle sectors by slave bosons. For a RISB representation describing superconductivity, we refer to Ref. [18].

In order to select the true complete physical states, composed of slave bosons and quasiparticles, the constraints

$$1 = \phi_E^\dagger \phi_E + \sum_{\sigma\sigma'} \phi_{\sigma\sigma'}^\dagger \phi_{\sigma'\sigma} + \phi_D^\dagger \phi_D, \tag{10}$$

$$f_\sigma^\dagger f_\sigma = \phi_D^\dagger \phi_D + \sum_{\sigma'} \phi_{\sigma\sigma'}^\dagger \phi_{\sigma'\sigma}, \tag{11}$$

$$f_\sigma^\dagger f_{\bar\sigma} = \sum_{\sigma'} \phi_{\bar\sigma\sigma'}^\dagger \phi_{\sigma'\sigma} \tag{12}$$

have to be enforced on each site i, whereby $\bar\sigma$ denotes the opposite spin projection to σ. The full electron operator is expressed through

$$\begin{aligned} \underline{c}_{i\sigma}^\dagger &= \frac{1}{\sqrt{2}} \sum_{\sigma'} \{\phi_{i\sigma\sigma'}^\dagger \phi_{iE} - (-1)^{\delta_{\sigma\sigma'}} \phi_{iD}^\dagger \phi_{i\bar\sigma\bar\sigma'}\}\, f_{i\sigma'}^\dagger \\ &\equiv \sum_{\sigma'} R_{i\sigma'\sigma}^\dagger\, f_{i\sigma'}^\dagger. \end{aligned} \tag{13}$$

The kinetic Hamiltonian $\mathcal{H}^{(\mathrm{kin})}$ is then readily written in RISB as

$$\underline{\mathcal{H}}^{(\mathrm{kin})} = -t \sum_{ij} \sum_{\sigma\sigma'\sigma''} R_{i\sigma'\sigma}^\dagger\, R_{j\sigma\sigma''}\, f_{i\sigma'}^\dagger f_{j\sigma''}. \tag{14}$$

Depending on the bosons, the R_i matrix relates the QP character to the full electron excitation on site i. To represent the local Hamiltonian, one uses the key fact that any local operator $\mathcal{O}$ may be written in quadratic terms of the bosonic degrees of freedom on the enlarged local Hilbert space, e.g., the four states in $\mathcal{A}$ as defined in (3). The general RISB form, with $(A|\mathcal{O}|A')$ represented as a matrix element in the basis set $\mathcal{A}$, is written as

$$\underline{\mathcal{O}} = \sum_{AA'} (A|\mathcal{O}|A') \sum_n \phi_{nA}^\dagger \phi_{A'n}. \tag{15}$$

For the local Hubbard interaction $\mathcal{H}_i^{(\mathrm{loc})}$ on each site, i.e., $\underline{\mathcal{O}} = U\underline{n}_{i\uparrow}\underline{n}_{i\downarrow}$, the slave-boson representation $\mathcal{H}_{\mathrm{U}} = U\phi_D^\dagger\phi_D$ is readily obtained. Together with the kinetic part, this completes the RISB single-band Hubbard Hamiltonian representation

$$\underline{\mathcal{H}} = -t \sum_{ij,\sigma\sigma'\sigma''} R_{i\sigma'\sigma}^\dagger\, R_{j\sigma\sigma''}\, f_{i\sigma'}^\dagger f_{j\sigma''} + U \sum_i \phi_{iD}^\dagger \phi_{iD}. \tag{16}$$

It is noted that as common in usual auxiliary-particle theories, there are inherent gauge symmetries. This can already be illustrated [40–42] using the most simplest slave-boson introduction from Eq. (1) by marking the U(1) gauge symmetry

$$\phi_i \to e^{i\theta_i}\phi_i, \qquad f_{i\sigma} \to e^{i\theta_i} f_{i\sigma}. \tag{17}$$

In specific cases, this symmetry may be used to gauge away the phases of the bosonic fields [43]. Furthermore, within single-orbital RISB on a given lattice site, an arbitrary SU(2) rotation of the QP operators provides some freedom in the representation of the corresponding QP indices. This holds also in the multiorbital case, but as shown in Ref. [17], physical observables remain of course generally gauge invariant. Let us mention that in this regard, Lanatà *et al.* [44] recently proposed an alternative RISB representation.

B. Saddle-point approximation and comparison to other many-body techniques

Enforcing the constraints (10)–(12) on each site in the thermodynamic limit, while keeping the operator character of the introduced electronic degrees of freedom appears unfeasible. Therefore, in most cases, slave-boson theory is actually practiced in its simplest nontrivial form, namely, within the saddle-point approximation. Its realization amounts to three essential steps [17]. First, the bosons are condensed to c numbers $\varphi_{An} \equiv \langle\phi_{An}\rangle$. Second, the constraints are treated on average by introducing Lagrange multipliers in a free-energy functional (see below). And third, the representation (13) of the physical electron operator has to be modified by a proper normalization in order to recover the correct noninteracting limit within the given mean-field picture.

With inverse temperature $\beta = 1/T$ and transformation of the kinetic part to k space with dispersion $\varepsilon_{\mathbf{k}}$, the saddle point is obtained from the free-energy functional [17]

$$\begin{aligned} &\Omega[\{\varphi_{An}\}; \Lambda, \lambda_0] \\ &\quad = -\frac{1}{\beta} \sum_{\mathbf{k}} \operatorname{tr} \ln \left[1 + \mathrm{e}^{-\beta\left(\mathbf{R}^\dagger(\varphi)\varepsilon_{\mathbf{k}}\mathbf{R}(\varphi) + \Lambda\right)}\right] - \lambda_0 \\ &\qquad + \sum_{AA'nn'} \varphi_{An'}^* \Bigg\{ \delta_{nn'}\delta_{AA'}\,\lambda_0 + \delta_{nn'}(A|\mathcal{H}^{\mathrm{loc}}|A') \\ &\qquad - \delta_{AA'} \sum_{\sigma\sigma'} \Lambda_{\sigma\sigma'}(n|f_\sigma^\dagger f_{\sigma'}|n') \Bigg\} \varphi_{A'n}, \end{aligned} \tag{18}$$

through extremalizing over the set $\{\varphi_{An}\}$ and the Lagrange multipliers. Note that λ_0 is associated with the constraint (10) and Λ deals with the remaining constraints (11) and (12).

Importantly, the physical self-energy takes on the form

$$\mathbf{\Sigma}(\omega) = \omega(1 - [\mathbf{R}\mathbf{R}^\dagger]^{-1}) + [\mathbf{R}^\dagger]^{-1}\mathbf{\Lambda}\mathbf{R}^{-1} - [\boldsymbol{\varepsilon}^0], \tag{19}$$

with ε^0 as the onsite part of the dispersion. Hence, the self-energy consists of a term linear in frequency as well as a static part, and the local QP weight $Z \equiv [1 - \frac{\partial}{\partial\omega}\Sigma\,]_{\omega=0}^{-1}$ is here generally given in matrix form via $\mathbf{Z} = \mathbf{R}\mathbf{R}^\dagger$. For the rest of the paper, we will discuss RISB by assuming that the mean-field limit is taken in the final equations. In this respect, to simplify notations, we thus also keep the ϕ notation for the slave bosons throughout the writing and will not furthermore highlight the difference to the condensed φ quantity.

We now try to classify briefly the performance of RISB on a qualitative level in view of some other available many-body techniques on the lattice. The self-energy is local, but carries frequency dependence, contrary to simplest Hartree-Fock for the Hubbard model. The optimal local many-body theory is given by dynamical mean-field theory (DMFT) (see, e.g., Refs. [45,46] for reviews). This theory describes a most general ω dependence within the context of a mapping of the correlated lattice problem onto the problem a quantum impurity residing within a self-consistent bath. The full-frequency information may be extracted via, e.g., quantum Monte Carlo or exact-diagonalization impurity solvers. The linear-frequency restriction of RISB allows one to study only Fermi-liquid regimes and spectral-weight transfer to, e.g., Hubbard bands is not accessible from the spectral function. Yet importantly, via an inspection of the occupation of the local states, still relevant information on the high-energy physics may be obtained. In principle, the slave-boson approach can also be interpreted as a simplified impurity solution within DMFT since the RISB formalism may also be implemented within a quantum-impurity-in-bath scope [24]. Let us note here that there are also differences concerning the level of approximation among the different available auxiliary-particle schemes since this often raises some confusion. For instance, interacting five-orbital Hamiltonians may be straightforwardly encountered by mean-field representations of Kotliar-Ruckenstein slave bosons [9] or slave spins [16] since those approaches enable a simplified treatment of the problem. In the more elaborate RISB method, such large orbital manifolds require special advancements, as discussed in this work.

Going beyond the local-self-energy concept is generally tough and we here do not want to enter this branch of many-body theory by general means. Let us note that there are rare slave-boson formulations beyond the mean-field limit, usually by invoking Gaussian fluctuations around the saddle point (see, e.g., Refs. [47,48]) in selected single-orbital problems. Such formulations are capable of describing k-dependent parts of the self-energy. But, to our knowledge so far no such advancement has been undertaken for the general RISB framework. Deriving and putting into practice a generic multiorbital slave-boson scheme beyond saddle-point proves technically very demanding. Cluster self-energies coping with short-range nonlocal correlations have been introduced to extended DMFT (see, e.g., Ref. [49] for a review), and the RISB method can indeed also be formulated within a cluster scheme [17,24,25]. It yields very good results in comparison to more elaborate cluster DMFT [24]. Here, however, we remain throughout the paper within the single-site framework.

III. MULTIORBITAL HAMILTONIANS

In this study, the multiorbital Hamiltonians are composed of a kinetic part and a local part that includes the electron-electron interaction, thus again of the general form (2), $\mathcal{H} = \mathcal{H}^{(\text{kin})} + \sum_i \mathcal{H}_i^{(\text{loc})}$. We here will model orbital manifolds with angular momentum $l = 1,2$, i.e., p- and d-shell systems.

A. Kinetic Hamiltonian

Electrons in M orbitals of Wannier type on the dim = three-dimensional simple-cubic lattice are considered. The kinetic Hamiltonian with only nearest-neighbor hopping t reads as

$$\mathcal{H}^{(\text{kin})} = -t \sum_{\langle ij\rangle m\sigma} c^{\dagger}_{im\sigma} c_{jm\sigma}, \tag{20}$$

using $m = 1,\ldots,M$. Note that we do not allow hopping between different orbital flavors. For the rest of the paper, the half-bandwidth $W/2$ is the unit of energy. Since the present kinetic Hamiltonian is diagonal in orbital space with identical eigenvalues for all orbitals, it remains invariant under orbital rotations.

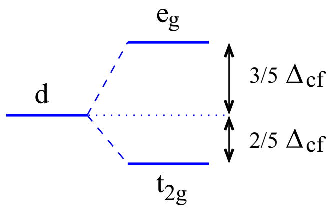

FIG. 1. Example for crystal-field splitting in the case of a d level in cubic symmetry. It splits into twofold $e_g = \{z^2, x^2 - y^2\}$ and threefold $t_{2g} = \{xz, yz, xy\}$. The level center is not changed.

B. Local Hamiltonian

On the local level of a single-lattice site, the respective Hamiltonian part is given by

$$\mathcal{H}^{(\text{loc})} = \mathcal{H}^{(\text{cf})} + \mathcal{H}^{(\text{int})} + \mathcal{H}^{(\text{SOC})}, \tag{21}$$

whereby the first term describes the crystal-field (cf) term, the second the Coulomb interaction (int), and the third the spin-orbit coupling (SOC). The single-particle crystal-field Hamiltonian takes care of a possible onsite energy splitting Δ_m between the orbitals (see Fig. 1), reading as

$$\mathcal{H}^{(\text{cf})} = \sum_{m\sigma} \Delta_m \, c^{\dagger}_{m\sigma} c_{m\sigma}. \tag{22}$$

1. *Slater-Condon form of the local interaction*

For the case of a complete rotational-invariant treatment on the local level, the corresponding two-particle interaction is described by the Slater-Condon (SC) Hamiltonian

$$\mathcal{H}^{(\text{int})} = \frac{1}{2} \sum_{\substack{m_1 m_2 \\ m_3 m_4}} \sum_{\sigma\sigma'} U_{m_1 m_2 m_3 m_4} c^{\dagger}_{m_1\sigma} c^{\dagger}_{m_2\sigma'} c_{m_4\sigma'} c_{m_3\sigma}. \tag{23}$$

Since we aim at a canonical modeling, we assume spherical symmetry of the electron-electron interaction throughout this work, i.e., no orbital-dependent screening mechanism is allowed. Then, the Coulomb matrix element is expressed via standard Slater integrals F^k through

$$U_{m_1 m_2 m_3 m_4} = \sum_{k=0}^{2l} a_k(m_1,m_2,m_3,m_4)\, F^k, \tag{24}$$

with expansion coefficients a_k given by

$$\begin{aligned} a_k(m_1,m_2,m_3,m_4) &= \sum_{q=-k}^{k} (2l+1)^2 (-1)^{m_1+q+m_2} \begin{pmatrix} l & k & l \\ 0 & 0 & 0 \end{pmatrix}^2 \\ &\quad \times \begin{pmatrix} l & k & l \\ -m_1 & q & m_3 \end{pmatrix} \begin{pmatrix} l & k & l \\ -m_2 & -q & m_4 \end{pmatrix}. \end{aligned} \tag{25}$$

In the case of p and d electrons, the relevant Slater integrals may be parametrized by averaged Coulomb integrals, namely, the Hubbard U and the Hund's exchange J_{H} as

$$l=1: \quad F^0=U,\, F^2=5J_{\mathrm{H}}, \tag{26}$$

$$l=2: \quad F^0=U,\, F^2=\frac{14}{1+r}J_{\mathrm{H}},\, F^4=rF^2. \tag{27}$$

The F^4/F^2 Slater-integral ratio is here chosen as $r=0.625$, which is adequate for transition-metal atoms.

2. Slater-Kanamori form of the local interaction

Treating full rotational invariance in the interactions was a long-standing problem in many-body techniques. Therefore, simpler versions of interacting Hamiltonians have been introduced. In the context of local Coulomb interactions, the Slater-Kanamori (SK) Hamiltonian is the most prominent one. It reads as

$$\begin{aligned}\mathcal{H}^{(\mathrm{int})} &= U\sum_m n_{m\uparrow}n_{m\downarrow} \\ &\quad+\frac{1}{2}\sum_{m\neq m',\sigma}\Big\{(U-2J_{\mathrm{H}})\,n_{m\sigma}n_{m'\bar{\sigma}}+(U-3J_{\mathrm{H}})\,n_{m\sigma}n_{m'\sigma} \\ &\quad+J_{\mathrm{H}}(c^{\dagger}_{m\sigma}c^{\dagger}_{m'\bar{\sigma}}c_{m\bar{\sigma}}c_{m'\sigma}+c^{\dagger}_{m\sigma}c^{\dagger}_{m\bar{\sigma}}c_{m'\bar{\sigma}}c_{m'\sigma})\Big\} \\ &=(U-3J_{\mathrm{H}})\frac{N(N-1)}{2}+\frac{5}{2}J_{\mathrm{H}}N-2J_{\mathrm{H}}S^2-\frac{1}{2}J_{\mathrm{H}}L^2.\end{aligned} \tag{28}$$

Here, $n=c^{\dagger}c$, and N marks the total-particle operator, S the spin operator, and L the orbital-momentum operator. This form of the local interaction is obtained from the general Slater-Condon form (23) via the restriction to only two-orbital interaction terms and the setting

$$\begin{aligned} U_{mmmm}&=U, & U_{mm'mm'}&=U-2J_{\mathrm{H}}, \\ U_{mm'm'm}&=J_{\mathrm{H}}, & U_{mmm'm'}&=J_{\mathrm{H}}.\end{aligned} \tag{29}$$

Although reduced, the Slater-Kanamori Hamiltonian is rotational invariant in the case of the p shell as well as the e_g and t_{2g} subshells of d-electron manifolds. However, it differs in the scaling of the local Coulomb interaction when compared to the SC form. In fact, the SC Hamiltonian takes on the SK operator structure, if the F^4/F^2 Slater-integral ratio is set to a formal, rather unphysically large value $r=1.8$.

C. Spin-orbit coupling

Spin and orbital momentum of an electron are coupled due to relativistic effects. The Hamiltonian expressing this coupling reads as

$$\mathcal{H}^{(\mathrm{SOC})}=\frac{\lambda}{2}\sum_{k=x,y,z}\sum_{\mu\mu'}\sum_{\sigma\sigma'}\tilde{L}^k_{\mu\mu'}\,\mathcal{S}^k_{\sigma\sigma'}\,c^{\dagger}_{\mu\sigma}c_{\mu'\sigma'}, \tag{30}$$

whereby $\tilde{L}$ denotes the angular-momentum representation on the l_z states and $\mathcal{S}$ carries the Pauli matrices as components and λ is the spin-orbit interaction constant. Because of the mixing of spin and orbital degrees of freedom, the spin-orbit Hamiltonian does generally not commutate with S^2 and L^2 in many-electron systems. However, it commutates with the total angular-momentum operator J^2 as well as its z component J_z.

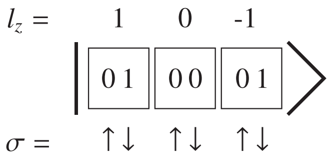

FIG. 2. Example for an initial state for a three-orbital p-shell model. This state represents two electrons, one in the $l_z=1$ spin-down orbital, the second one in the $l_z=-1$ spin-down orbital. By construction, these states diagonalize the operators L_z and S_z.

IV. MULTIORBITAL SLAVE BOSONS

A. States and operators

In the following, three building blocks of the local multiorbital rotational-invariant representation of the slave-boson formalism are introduced. First, the local many-body Hilbert space in Fock-basis representation. Second, a set of commutating quantum operators which can be represented on that space which fully and uniquely determine the different states. And, third, a matrix containing all state-connecting variational parameters. The latter will be determined such that it follows the given symmetries of the system and may ultimately be used as the slave-boson operator matrix Φ.

The first building block of the M-orbital rotationally invariant representation is the local many-body Hilbert space at one space-point entity i spanned by the set $\mathcal{Q}=\{\mathbf{v}_1,\ldots,\mathbf{v}_a,\ldots,\mathbf{v}_Q\}$ of $Q=2^{2M}$ vectors, such that renormalizations between adjacent space points are excluded. It contains, for example, all possible local many-body d states or, in a cluster scheme, all possible many-electron configurations of a four-site plaquette. The vectors $\mathbf{v}_a$ describe two spin-resolved orbitals for every local-orbital degree of freedom. Each one may either be occupied (represented by 1) or empty (represented by 0), which is nothing but a Fock-space occupation-number representation of all configurations over a body of binary numbers $\mathbb{B}$, i.e., $\mathbf{v}_a\in\mathbb{B}^{2M}$. Thus, each vector has $2M$ entries, which, e.g., in the case of an atomic shell with angular momentum l amounts to $2(2l+1)$. An example for $M=3$, a p-shell state, is shown in Fig. 2. Since the size of $\mathcal{Q}$ scales like $Q=2^{2M}$, matrices represented in this space become large for $M>3$ and numerical computation becomes costly in time and memory. It is worthwhile to use symmetries to rule out states that do not take part in local interaction processes and hence reduce the size of the problem.

This leads to the second building block of the advanced RISB formalism, namely, the set $\mathfrak{S}$ of local-commutating operators. In the absence of spin-orbit coupling, it is chosen to consist of the particle-number operator N, spin square S^2, and spin-z-component operator S_z, the seniority operator Ξ which measures the number of unpaired spins in a given state, the orbital angular momentum L^2, and orbital-angular-momentum z-component operator L_z, i.e., $\mathfrak{S}:=\{N,S^2,S_z,\Xi,L^2,L_z\}$. The set $\mathfrak{S}$ is easily represented on $\mathcal{Q}$ via explicitly considering the operator action on the state vectors. In the following, we always assume the initial Fock-space orbitals to be labeled with magnetic quantum numbers l_z and spin quantum number s_z from highest to lowest value (e.g., $l=1\rightarrow 1\uparrow,1\downarrow,0\uparrow,0\downarrow,-1\uparrow,-1\downarrow$), thus diagonalizing the operators L_z and S_z by construction (cf. Fig 2). The particle-number operator is most easily represented on these states. It is by construction also diagonal in the occupation-number basis and counts the number of occupied orbitals, thus, electrons. For the matrix representation of the S^2 operator between vectors $\mathbf{v}_a,\mathbf{v}_b$, the expression

$$(S^2)_{ab} = \langle \mathbf{v}_a| \sum_{k=x,y,z} \sum_{\sigma_1\sigma_2\sigma_3\sigma_4} \times \sum_{\mu_1\mu_2} \mathcal{S}^k_{\sigma_1\sigma_2}\mathcal{S}^k_{\sigma_3\sigma_4} c^\dagger_{\mu_1\sigma_1} c_{\mu_1\sigma_2} c^\dagger_{\mu_2\sigma_3} c_{\mu_2\sigma_4}|\mathbf{v}_b\rangle \tag{31}$$

holds, with local orbital indices μ_1,μ_2 and Pauli matrices $\mathcal{S}$. For the S_z operator it follows

$$(S_z)_{ab} = \langle \mathbf{v}_a| \sum_{\mu}\sum_{\sigma_1\sigma_2} \mathcal{S}^z_{\sigma_1\sigma_2} c^\dagger_{\mu\sigma_1} c_{\mu\sigma_2}|\mathbf{v}_b\rangle. \tag{32}$$

For the L^2 and L_z operators hold similar relations as for the spin operators, namely,

$$(L^2)_{ab} = \langle \mathbf{v}_a| \sum_{k=x,y,z} \sum_{\mu_1\mu_2\mu_3\mu_4} \times \sum_{\sigma} \tilde{L}^k_{\mu_1\mu_2}\tilde{L}^k_{\mu_3\mu_4} c^\dagger_{\mu_1\sigma} c_{\mu_2\sigma} c^\dagger_{\mu\sigma} c_{\mu\sigma}|\mathbf{v}_b\rangle \tag{33}$$

and

$$(L_z)_{ab} = \langle \mathbf{v}_a| \sum_{\sigma}\sum_{\mu_1\mu_2} \tilde{L}^z_{\mu_1\mu_2} c^\dagger_{\mu_1\sigma} c_{\mu_2\sigma}|\mathbf{v}_b\rangle. \tag{34}$$

Writing out the matrix elements for the seniority operator Ξ in second quantization is a bit more involved and can be found in the literature [50,51] in terms of vector-coupled ladder operators of two spins at zero net momentum.

A common eigenbasis $\mathcal{A}$, the so-called adapted basis, for all operators in $\mathfrak{S}$ has to be generated. It is spanned by the vectors $\mathbf{A}_A$, of which there are again Q with index $A \in [1,\ldots,Q]$. They are conveniently labeled as $|A\rangle = |\nu,s,\sigma,\xi,l,l_z\rangle \in \mathbb{C}^{2M}$. These six quantum numbers are sufficient to label the states of the local Hilbert space up to five orbitals ($M = 5$) unambiguously. After the diagonalization process, the states are ordered with left quantum numbers varying slowest, right fastest, starting from lowest values to highest. The basis is stored as a unitary transformation matrix $\mathcal{U}_\mathcal{A}$, which transforms all operators represented in Fock space $\mathcal{Q}$ to the adapted basis as a linear combination of the previous occupation-number representation with coefficients of complex-number kind.

The central building block, the slave-boson operator Φ, may now be be seen as a transition operator, that mediates between the quasiparticle and local-excitation degree of freedom. Conveniently, it can be expressed with the same set of possible local states $|A\rangle = |\nu_A,s_A,\sigma_A,\xi_A,l_A,l_{zA}\rangle$ and $|B\rangle = |\nu_B,s_B,\sigma_B,\xi_B,l_B,l_{zB}\rangle$. Hence, it carries two indices and is represented as a matrix on the local Hilbert space of the adapted-basis-set states, i.e., $\Phi_{AB} \in \mathcal{C}^{Q\times Q}$. The specific action of the operator Φ_{AB} is, however, unknown *a priori* and has to be determined self-consistently in the saddle-point approximation, with its matrix elements as parameters. Thus, the number of slave-boson parameters in the RISB calculation scales like $n_\phi = Q^2$.

B. Rotationally invariant representation

Let us for the following use a common index $\alpha = \{m,\sigma\}$ for orbital and spin-projection degrees of freedom. By rearranging Eq. (15) with the help of the unitary transformation matrix $\mathcal{U}_\mathcal{A}$, one obtains a representation which is by construction basis free, hence obviously invariant under unitary rotations [52]:

$$\begin{aligned}\underline{\mathcal{O}} &= \sum_{AA'}(A|\mathcal{O}|A')\sum_n \phi^\dagger_{nA}\phi_{A'n} = \sum_{nAA'}\phi^\dagger_{nA}(A|\mathcal{O}|A')\phi_{A'n}\\ &= \mathrm{Tr}(\phi^\dagger\mathcal{O}\phi) = \mathrm{Tr}(U_\mathcal{A}U^\dagger_\mathcal{A}\phi^\dagger U_\mathcal{A}U^\dagger_\mathcal{A}\mathcal{O}U_\mathcal{A}U^\dagger_\mathcal{A}\phi)\\ &= \mathrm{Tr}(U^\dagger_\mathcal{A}\phi^\dagger U_\mathcal{A}U^\dagger_\mathcal{A}\mathcal{O}U_\mathcal{A}U^\dagger_\mathcal{A}\phi U_\mathcal{A}) = \mathrm{Tr}(\bar{\phi}^\dagger\bar{\mathcal{O}}\bar{\phi}).\end{aligned} \tag{35}$$

The renormalization matrices from Eq. (13) are generalized in the multiorbital mean-field framework via

$$c_\alpha \rightarrow \sum_\beta R_{\beta\alpha}f_\beta, \qquad c^\dagger_\alpha \rightarrow \sum_\beta R^*_{\alpha\beta}f^\dagger_\beta, \tag{36}$$

whereby

$$R^*_{\alpha\beta} = \sum_\gamma T^*_{\alpha\gamma}w_{\gamma\beta} \tag{37}$$

with (see Appendix A)

$$T^*_{\alpha\gamma} = \mathrm{Tr}(\phi^\dagger f^\dagger_\alpha\phi c_\gamma), \tag{38}$$

and a normalization matrix w, which carries the matrix square root of the product of the local particle- and hole-density matrix (see Ref. [17] for details). Introducing that matrix ensures the correct mean-field regime of RISB.

Finally, the multiorbital constraints at saddle point compactly read as

$$\mathrm{Tr}(\phi^\dagger\phi) = 1, \tag{39}$$

$$\mathrm{Tr}(\phi f^\dagger_\alpha f_\beta\phi^\dagger) = \langle f^\dagger_\alpha f_\beta\rangle. \tag{40}$$

C. First glance on symmetry reduction

An obvious way to reduce the number of parameters in the problem is by the use of the symmetries of the local interaction. Hence, one may cut out slave-boson amplitudes, which would otherwise violate a given symmetry. This renders the slave-boson operator block diagonal in the allowed combinations of quantum numbers. For instance, let the particle-number conservation be a symmetry of the local Hamiltonian, i.e., the commutator $[\mathcal{H},N]$ vanishes. Then, all slave-boson amplitudes ϕ_{AB} with $n(A) \neq n(B)$ will also be zero. This is known *a priori*, so those amplitudes can be ruled out and be excluded in solving the saddle-point problem. This does not only render the Φ matrix sparse (and block diagonal) from the beginning, it also enables to reduce the number of saddle-point equations, which are nothing but derivatives of the free-energy functional with respect to the free parameters of the formalism.

In previous implementations of RISB, all operations were iterated over such irreducible quantum-number subspaces, which made it hard to change from one set of quantum numbers (or model) to another. A different approach shall be presented here, which not only focuses on the sparsely populated structure of the matrices under rotation to an adapted basis, but also opens the path to use the lattice point-group symmetry to further reduce the number of free parameters.

D. Top-down reduction of free parameters

The number of free parameters can be further reduced, if the point-group symmetry of the lattice is to be imprinted on the local-interacting Hilbert space. Just as the Pauli matrices are, for example, a matrix basis set for the four-dimensional real vector space of all complex-Hermitian 2×2 matrices, one can find a matrix basis set obeying a certain point-group symmetry. This enables then the spanning of space of all complex matrices compliant with that given symmetry. If that point-group symmetry is a symmetry of the lattice under consideration, it rules out certain many-body transitions, which in turn are here represented by the slave-boson operator. This makes it possible to represent the slave-boson operator in a basis set which only allows for point-group-supported transitions in the first place.

The idea of expanding an operator representation in a basis of orthonormal matrices obeying a finite symmetry group [53] is already used in the context of an implementation of the Gutzwiller formalism [5]. There, it is done for the case of paramagnetic problems [54] for d orbitals and with further reduction by symmetry of the involved renormalization matrices. The latter are then promoted to free variables to treat spin-orbit coupling and crystal-field splitting in f-orbital systems [44,55]. In the following, the details of an implementation without the need of promoting the renormalization matrices to free variables is wrapped up.

The goal is a decomposition of the represented slave-boson operator Φ into a number of Y basis matrices $\tilde{\Phi}_i$ within the adapted basis $\mathcal{A}$ of the form [56]

$$\Phi = p_1\tilde{\Phi}_1 + p_2\tilde{\Phi}_2 + \cdots + p_Y\tilde{\Phi}_Y = \sum_{i=1}^{Y} p_i\,\tilde{\Phi}_i, \tag{41}$$

with coefficients $p_i \in \mathbb{C}$, and the orthonormality relation

$$\delta_{ij} = \langle\tilde{\Phi}_i\,\tilde{\Phi}_j\rangle := \mathrm{Tr}(\tilde{\Phi}_i^\dagger\,\tilde{\Phi}_j). \tag{42}$$

Their indices are still labeled by the vectors of the adapted basis $\mathcal{A}$. The basis matrices $\tilde{\Phi}_i$ can be constructed in a way that they obey a certain point-group symmetry G. They commute with all elements $g^{\mathcal{A}}$ of the symmetry group, represented in $\mathcal{A}$. That also means that this expansion of Φ projects its action on a subspace which is commensurable with the symmetry group. All other action is lost. The generation of $\tilde{\Phi}_i$ is described in Appendix B.

Inserting the given expansion into the general equation (35) for the slave-boson representation of operator $\mathcal{O}$ results in

$$\begin{aligned}\underline{\mathcal{O}} &= \mathrm{Tr}\left(\sum_i p_i^*\tilde{\Phi}_i^\dagger\bar{\mathcal{O}}\sum_j p_j\tilde{\Phi}_j\right) = \sum_{ij} p_i^*\,\mathrm{Tr}(\tilde{\Phi}_i^\dagger\bar{\mathcal{O}}\tilde{\Phi}_j)\,p_j\\ &= \mathbf{p}^\dagger\,\mathrm{Tr}(\Phi^\dagger\bar{\mathcal{O}}\Phi)\,\mathbf{p} = \mathbf{p}^\dagger\,O\,\mathbf{p}.\end{aligned} \tag{43}$$

In this form, one precomputes and stores the matrices

$$(T^*_{\alpha\gamma})^{ij} := \mathrm{Tr}(\tilde{\Phi}_i^\dagger f_\alpha^\dagger\tilde{\Phi}_j c_\gamma), \tag{44}$$

$$\left(\Delta^{(p)}_{\alpha\beta}\right)^{ij} := \mathrm{Tr}(\tilde{\Phi}_i^\dagger f_\alpha^\dagger f_\beta\tilde{\Phi}_j), \tag{45}$$

$$(\mathcal{H}^{(\mathrm{loc})})^{ij} := \mathrm{Tr}(\tilde{\Phi}_i^\dagger\mathcal{H}^{(\mathrm{loc})}\tilde{\Phi}_j), \tag{46}$$

$$(N_{\alpha\beta})^{ij} := \mathrm{Tr}(\tilde{\Phi}_i f_\alpha^\dagger f_\beta\tilde{\Phi}_j^\dagger), \tag{47}$$

so that for the constraints follows

$$\mathrm{Tr}(\phi^\dagger\phi) = \sum_{ij} p_i^*\mathrm{Tr}(\tilde{\Phi}_i^\dagger\tilde{\Phi}_j)p_j = \sum_i p_i^* p_i = 1, \tag{48}$$

$$\mathrm{Tr}(\phi f_\alpha^\dagger f_\beta\phi^\dagger) = \sum_{ij} p_i(N_{\alpha\beta})^{ij}p_j^* = \langle f_\alpha^\dagger f_\beta\rangle. \tag{49}$$

The free-energy functional is then rewritten as

$$\begin{aligned}\Omega[p_i^*,\Lambda^*,\lambda_0^*] = &-\frac{1}{\beta}\sum_{\mathbf{k}}\mathrm{Tr}\,\ln[1+e^{-\beta[\mathbf{R}^\dagger\epsilon_{\mathbf{k}}\mathbf{R}+(\Lambda+\mathrm{H.c.})]}]\\ &-\left[\lambda_o^*\left(1-\sum_i p_i^* p_i\right)\right]\\ &-\left[\Lambda^*_{\beta\alpha}\sum_{ij}p_i(N_{\alpha\beta})^{ij}p_j^* + \mathrm{c.c.}\right]\\ &+\sum_{ij}p_i^*(\mathcal{H}^{\mathrm{loc}})^{ij}p_j.\end{aligned} \tag{50}$$

We expect the functional to map the complex variables $z := \{p_i,\Lambda,\lambda_0\}$ to a real number $\Omega \in \mathbb{R}$. So, for writing the saddle-point equations, the formal derivative of the functional Ω with respect to the complex conjugate of all variables $\partial\Omega/\partial z^*$ is taken. By using Wirtinger calculus [57], the saddle-point equations for the real and imaginary parts of the functional read as

$$\frac{\partial\Omega}{\partial\,\mathrm{Re}\,z^*} = 2\,\mathrm{Re}\frac{\partial\Omega}{\partial z^*} \overset{!}{=} 0, \tag{51}$$

$$\frac{\partial\Omega}{\partial\,\mathrm{Im}\,z^*} = 2\,\mathrm{Im}\frac{\partial\Omega}{\partial z^*} \overset{!}{=} 0. \tag{52}$$

Technical remarks on the top-down approach are as follows. One starts with an exhaustive list of quantum numbers for labeling the occurring states. For a general p-shell problem, the problem consists of labeling 64 states, which can be unambiguously described by the five quantum numbers ν, s, s_z, l, and l_z. For a d shell, the seniority quantum number ξ, which counts the number of unpaired spins in a given state, has to be added to label the occurring $2^{10} = 1024$ states unambiguously. Since we exclude the effect of superconductivity, we first abandon mixing between states of different particle number, rendering ν a good quantum number. We then apply the point-group symmetry to assort states with point-group-compliant combinations of l and l_z. They are not straightforwardly good quantum numbers since, e.g., the local interaction may mix different states of l_z. But, due to the underlying point-group symmetry, only specific mixings are allowed. In the next step, the mixing of different values of s, the total spin momentum, shall be preserved. This still leaves s_z as a free parameter and enables us at this stage to locally describe magnetism along a spin-quantization axis. However, since at this stage we are only interested in paramagnetic solutions, the number of parameters may still be reduced. In a paramagnetic saddle-point solution, we expect the variational parameter belonging to a spin multiplet ϕ_{s_z}, with $s_z = -s, \ldots, s$, to be identical for all s_z values. Using this requirement, it is sufficient to average the connection matrices beforehand via $\phi = \frac{1}{\sqrt{2s+1}} \sum_{s_z=-s}^{s} \phi_{s_z}$ and compute the saddle-point solution only for the symmetrized parameter.

E. Double groups for spin-orbit coupling

For the inclusion of spin-orbit coupling, it is necessary to expand the local symmetry group from a normal point group to a double group, describing also the spin-direction change after a rotation about 2π. In addition, a new commutating set of local operators is used, S_z and L_z are replaced by the total angular-momentum operator J^2 and its z component J_z. This is put into practice by introducing a new rotation element $\bar{E}$ and extending the group by doubling its elements, i.e.,

$$\mathfrak{D}\, G = \{g, \bar{E}\, g\} \quad \forall g \in G. \tag{53}$$

The new double group consists of all group elements g of the previous group G plus all previous elements multiplied by $\bar{E}$. This changes also the available equivalence classes and amounts to noninteger values in the character tables.

F. Local correlation functions

The local-correlation operator on the full orbital space in magnetic-quantum-number representation (spherical harmonics) is of the form

$$\begin{aligned} \bar{O}_{\alpha\beta\gamma\delta} &:= \mathrm{Tr}(\phi^\dagger (\bar{O})_{\alpha\beta\gamma\delta} \phi) \\ &= \mathrm{Tr}(\phi^\dagger [(O^2)_{\alpha\beta\gamma\delta} - (O)_{\alpha\beta}(O)_{\gamma\delta}] \phi). \end{aligned} \tag{54}$$

It is rotated to the space of cubic harmonics by the transformation $\mathbf{K}$ with extraction of the diagonal elements for the physical interpretation, i.e.,

$$\bar{O}_{\alpha'\beta'} := \bar{O}_{\alpha'\alpha'\beta'\beta'} = K^\dagger_{\alpha'\alpha} K^\dagger_{\beta'\gamma} \bar{O}_{\alpha\beta\gamma\delta} K_{\beta\alpha'} K_{\delta\beta'}. \tag{55}$$

G. Further details on implementation and computation

The basis matrices depend only on the number of orbitals and point-group symmetry involved, so they can be precomputed and stored. For a given problem, also matrices like $(T_{\alpha\beta})^{ij}$ and $(N_{\alpha\beta})^{ij}$ can be precomputed. They depend on the geometry of the given model, but not on the values of the interaction parameters. Since all these matrices are very large but sparse, they are stored in *compressed column/row storage*. For every set of interaction parameters, only $(H^{(\mathrm{loc})})^{ij}$ needs to be recomputed.

Table I lists the number $n_\phi^{(\mathrm{red})}$ of free parameters after symmetry reduction for selected cases of orbital problems of size $M = \{3,5\}$. Let us also quickly mention the difference in the numerical effort compared to a standard density-density slave-boson calculation [e.g., via a straightforward Kotliar-Ruckenstein [9] (KR) implementation]. In RISB without symmetry constraints, the number of slave bosons amounts for a M-orbital problem to $n_\phi = 2^{4M}$, whereas there are $n_\phi = 2^{2M}$ bosons in the standard KR scheme focusing on the orbital-density labeling of the local states. Furthermore, RISB operates with matrix objects, while KR works with scalar quantities (e.g., an orbital-diagonal QP weight). Thus, there is a quadratic gain (with some problem-specific prefactor) when going from KR to RISB calculations. Note that in addition the memory demands are much more serious in a RISB computation

TABLE I. Examples for the number of parameters for different combinations of the orbital-manifold size M with point group G after reduction by symmetry. Note that for the here chosen applications, the different cubic groups O and O_{h} yield identical results.

M	Symmetry group G	$n_\phi^{(\mathrm{red})}$
3	O	16
3	$\mathfrak{D}\, O$	50
5	O	873
5	$\mathfrak{D}\, O$	2064
5	D_4	2516

In order to find the actual numerical solution of the RISB saddle-point equations, we use a parallelized and data-distributed implementation of the nonlinear-equation solver from Dennis and Schnabel with backtracking [58] as well as a problem-size adapted perturbation of the Hessian matrix.

The first-principles DFT data used in Sec. VI C stems from an implementation [59] of the mixed-basis pseudopotential formalism.

V. COMBINATION WITH DENSITY FUNCTIONAL THEORY

The RISB approach is not limited to sole model problems. It can be combined with density functional theory (DFT) to directly address correlated materials within a realistic first-principles setting. There are in principle two ways to facilitate such a DFT+RISB framework. First, in the so-called "one-shot" or "post-processing" scheme, the DFT Kohn-Sham Hamiltonian, expressed in a localized basis, replaces the noninteracting part of the model Hamiltonian. The interacting part is then again provided by a suitable Hubbard-type form, e.g., by the Slater-Condon Hamiltonian. Thus, the hoppings, crystal fields, and also spin-orbit terms may be taken over from the DFT calculations, and the complete problem is converged in the RISB formalism. However, there is no feedback of the correlation effects onto the electronic charge density. To achieve this, the second option, the so-called charge self-consistent (CSC) scheme, has to be employed. In the following, we want to briefly mark the essential steps of the DFT+RISB approach. Essentially, the general structure is very similar as for the known DFT+DMFT formalism and we hence refer to Refs. [60,61] for further details.

A converged Kohn-Sham self-consistency cycle of a DFT calculation for a periodic crystal yields the eigenenergies $\varepsilon_{\mathbf{k}\nu}$ and eigenfunctions $\psi_{\mathbf{k}\nu}$ for wave vector $\mathbf{k}$ and band ν in reciprocal space. A projection operator $P(\mathbf{k})$ enables the mapping of the Bloch (bl) states onto localized orbitals within a chosen energy window $\mathcal{W}$. The projection operator allows us to define the $\mathcal{W}$-restricted Kohn-Sham Hamiltonian in a localized basis, i.e.,

$$\mathcal{H}'(\mathbf{k}) := P(\mathbf{k})\, \mathcal{H}_{\mathrm{bl}}(\mathbf{k})\, P^\dagger(\mathbf{k}). \tag{56}$$

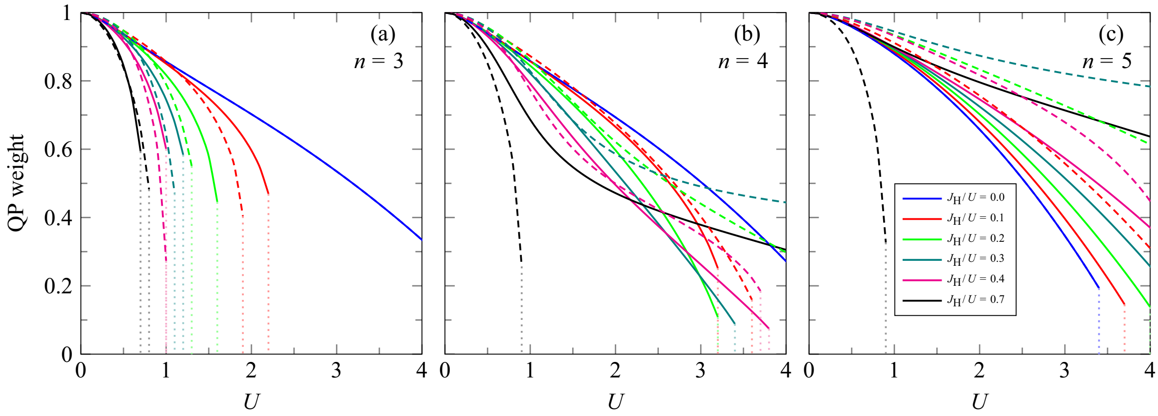

FIG. 3. Quasiparticle (QP) weight with respect to the Hubbard-interaction strength U for the degenerate three-orbital p-shell model at different fillings n and with different J_{H}/U ratios. Solid lines: Slater-Condon interaction; dashed lines: Slater-Kanamori interaction. The light dotted vertical lines are guides to the eyes for the critical U_c marking the Mott transition.

We separate the onsite terms from the truly k-dependent ones by defining

$$\mathcal{H}_0 := \frac{1}{N_k}\sum_{\mathbf{k}} \mathcal{H}'(\mathbf{k}) \tag{57}$$

and extract the realistic kinetic Hamiltonian in the localized basis via

$$\mathcal{H}^{(\mathrm{kin})}(\mathbf{k}) := \mathcal{H}'(\mathbf{k}) - \mathcal{H}_0. \tag{58}$$

Solving the RISB saddle-point equations yields the renormalized Hamiltonian

$$\mathcal{H}''(\mathbf{k}) = R^\dagger\, \mathcal{H}^{(\mathrm{kin})}(\mathbf{k})\, R + \Lambda, \tag{59}$$

which describes the "one-shot" solution of the combination with DFT.

In order to proceed to the CSC solution, the feedback onto the Bloch level is needed. This is achieved by replacing the interested DFT correlated part with the RISB correlated one in $\mathcal{H}_{\mathrm{bl}}$, reading as

$$\mathcal{H}_{\mathrm{bl}}^{(\mathrm{new})}(\mathbf{k}) = \mathcal{H}_{\mathrm{bl}}(\mathbf{k}) + P^\dagger(\mathbf{k})[\mathcal{H}''(\mathbf{k}) - \mathcal{H}'(\mathbf{k}) - \mathcal{H}_{\mathrm{dc}}]\, P(\mathbf{k}). \tag{60}$$

As in the DFT+DMFT framework [61], the double-counting term $\mathcal{H}_{\mathrm{dc}}$ takes care of the fact that part of the correlation is already included in DFT from the exchange-correlation functional. The fully localized double counting [62] is used in this work. Note that in the "one-shot" scheme the double counting may be absorbed in the chemical potential.

The particle number in the CSC scheme is fixed in the larger space of $\mathcal{H}_{\mathrm{bl}}(\mathbf{k})$ at every iteration. At each CSC step, one Kohn-Sham iteration and a self-consistent RISB calculation is performed. After each latter convergence, a charge-shifting matrix ΔN_{bl} is extracted as

$$\Delta N_{\mathrm{bl}} := P^\dagger\,(N_{\mathrm{RISB}} - N_{\text{Kohn-Sham}})\, P, \tag{61}$$

which is then fed back to the DFT charge-density calculation to recompute the Kohn-Sham potential for the next iteration step [61]. This procedure is repeated, until the CSC cycle converges. Note that ΔN_{bl} is a traceless matrix which reshuffles the charge due to the many-body correlations [61].

There are other CSC implementations with a similar many-body quality available, namely, a DFT+Gutzwiller approach [63,64] as well as the so-called Gutzwiller-DFT [65] method.

VI. RESULTS

The following sections are devoted to the application of the symmetry-adapted RISB formalism in the context of a multiorbital onsite interacting Hamiltonian. Main focus is on the interplay between the onsite Hubbard U and the Hund's exchange J_{H} with respect to the overall electron filling n. Whereas we first deal with minimal lattice models, the attention is shifted to the realistic context of the iron-chalcogenide systems FeSe and FeTe in the final part of this section.

As noted in Sec. III A, all model Hamiltonians in this work are explored on a simple-cubic lattice with nearest-neighbor hopping. Moreover, a Mott transition with increasing Hubbard U is here defined by the disappearance of the metallic state via a vanishing QP weight Z at a critical $U_c := U_{c2}$. The issue of metal-Mott phase coexistence [66] is not investigated in this work.

A. Three-orbital *p*-shell model

We start with an interacting three-orbital model having the complete symmetry of a $l = 1\,(p)$ manifold. Both rotational-invariant local-interaction Hamiltonians, i.e., of Slater-Condon and of Slater-Kanamori types, are utilized. The full cubic point group underlies the present problem.

Figure 3 displays the orbital-degenerate QP weight Z for different ratios J_{H}/U in the half-filled case $n = 3$ as well as the fillings $n = 4$ and 5. Comparing the results for the different electron counts on a global level, while for $J_{\mathrm{H}} = 0$ the correlation strength increases with rising n, for finite Hund's exchange it weakens in that direction. At half-filling, the critical U_c diminishes with growing J_{H}/U ratio [21], similar as in the two-orbital case [17,21]. On the contrary, for the case of $n = 4$ electrons in three orbitals, the well-known Janus physics [36,37] emerges at sizable J_{H}/U: the system becomes strongly correlated with substantially reduced Z already at intermediate U and the Mott transition is, on the other hand, shifted to rather large interaction strength. The fast reduction of Z is associated

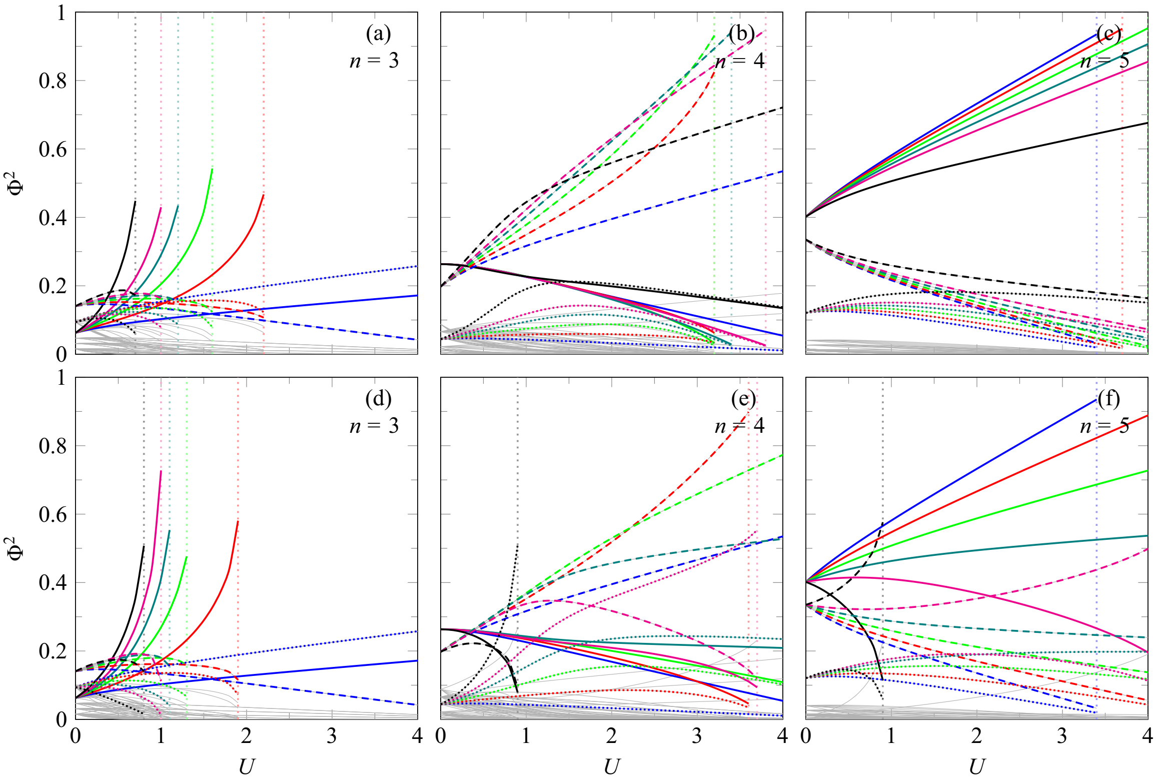

FIG. 4. Slave-boson amplitudes of dominant multiplets in the three-orbital model at different filling n. Top row: SC Hamiltonian; bottom row: SK Hamiltonian. Colors mark different $J_{\rm H}/U$, with the coding as in Fig. 3. (a), (d) solid line: ϕ_{10}; dashed line: ϕ_6; dotted line: ϕ_9. (b), (e) solid line: ϕ_{15}; dashed line: ϕ_{14}; dotted line: ϕ_{10}. (c), (f) solid line: ϕ_{15}; dashed line: ϕ_{16}; dotted line: ϕ_{14}. Classification of the multiplets ϕ_Γ can be found in Table II.

with the formation of large local magnetic moments triggered by $J_{\rm H}$. Notably, for the shown extreme case of $J_{\rm H}/U = 0.7$, the SC Hamiltonian still restores this phenomenology, whereas the SK form loses it because of the too strong negativity in some interaction terms. For $n = 5$, the Janus physics mostly disappears again and the differences between SC and SK are significant for any size of the Hund's exchange.

Importantly, the RISB framework not only provides information on the QP weight which triggers the band renormalization in reciprocal space, it also enables insight in the local real-space competition between relevant many-body multiplets via an analysis of the occupation hierarchy of the associated slave-boson amplitudes. As a first observation, for both interaction types, i.e., SC and SK, the same multiplets govern the physics described by RISB. This is expected because in the three-orbital model, both parametrizations obey the same complete symmetry, commutating with the set $\{N, S^2, S_z, \Xi, L^2, L_z\}$.

Figure 4 shows the slave-boson amplitudes for the dominant multiplet states at different fillings. In the case of $n = 3$, the Mott transition is driven by a one-dimensional spin quartet of symmetry class A_1 (see Table II), resembling Hund's rule. At the full-localization transition, this local many-body state with three unpaired spins is the only remaining one. For $n = 4$ and 5, the local physics of the system is dominated by the three-dimensional T_1 multiplets. In the four-particle sector, it corresponds to a spin triplet with two unpaired spins, while in the five-particle sector to a spin doublet with only one unpaired spin. The $n = 4$ Janus-face behavior with increasing U is associated with a stronger flattening of the four-particle T_1 in combination with a near degeneracy of the three-particle A_1 and the five-particle T_1, best illustrated for $J_{\rm H}/U = 0.7$ (0.3) in the SC (SK) case. Hence, symmetric fluctuations from the four-particle sector to the three-/five-particle sector are uniquely underlying the Janus-face physics.

TABLE II. Classification of dominant slave-boson amplitudes associated with local multiplets as plotted in Fig. 4 for the three-orbital model. Notation is as follows: Γ is an internal label for the slave-boson number. $\mathcal{C}: \sum_{\sigma=-s}^{s}(N,s,\sigma,\{\nu\},\{l\},\{l_z\})$, where curly brackets indicate sets as imprinted by the point-group symmetry class $\mathcal{C}$. All sums are normalized by a factor $\sqrt{2s+1}$. The number of nonzero elements refers to each spin-sum term in the classification symbol. For the whole number of nonzero elements in ϕ_Γ, it has to multiplied by $2s + 1$.

Γ	Symmetry	Nonzero
6	T_1: $\sum_{\sigma=-1}^{1}(2,1,\sigma,2,1,\{-1,0,1\})$	3
9	T_2: $\sum_{\sigma=-1/2}^{1/2}(3,1/2,\sigma,3,2,\{-2,-1,0,1,2\})$	6
10	A_1: $\sum_{\sigma=-3/2}^{3/2}(3,3/2,\sigma,3,0,0)$	1
14	T_1: $\sum_{\sigma=-1}^{1}(4,1,\sigma,2,1,\{-1,0,1\})$	3
15	T_1: $\sum_{\sigma=-1/2}^{1/2}(5,1/2,\sigma,1,1,\{-1,0,1\})$	3
16	A_1: (6,0,0,0,0,0)	1

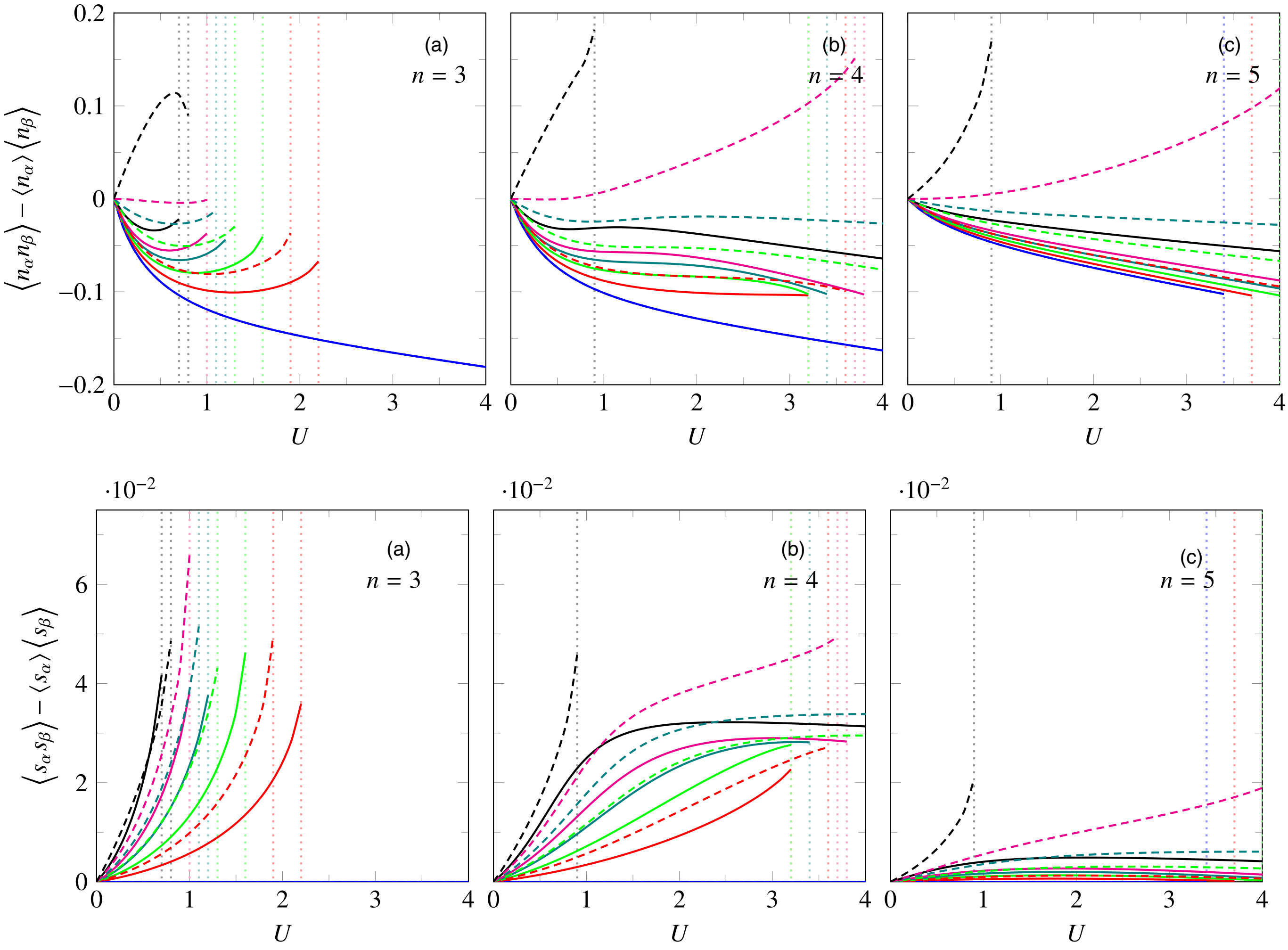

FIG. 5. Off-diagonal ($m \neq m'$) onsite correlation function of the three-orbital model for charge (top) and spin (bottom). Solid lines: Slater-Condon interaction; dashed lines: Slater-Kanamori interaction. Colors mark different J_H/U, with the coding as in Fig. 3.

To shed further light on the the fluctuations, we plot the onsite charge- and spin-correlation functions between the degenerate orbitals in Fig. 5. Charge correlations are negative for the proper realistic repulsion physics of the multiorbital Hubbard Hamiltonian, which is always ensured by the SC Hamiltonian. Due to the restricted Hilbert space, the fluctuations are smallest in magnitude for filling $n = 5$. Because of the Hund's rule, onsite spin fluctuations between orbitals are positive in sign. Only for $J_H = 0$ the pathological case of uncorrelated spins sets in. For $n = 4$ the correlation functions exhibit plateaulike appearance for U values in the Janus-face regime, again most obviously realized for $J_H/U = 0.7$ (0.3) in the SC (SK) case. This enables J_H as the dominant relevant energy scale in that regime, and a rather irrelevant influence of moderate changes of U.

B. Five-orbital *d*-shell model

Let us turn to the case of five interacting orbitals on the cubic lattice. Because of the highly enlarged Hilbert space compared to the three-orbital scenario, the introduced symmetry considerations are now truly indispensable for a computational study of such a manifold. Three cases are explored, namely, the orbital-degenerate, the more realistic problem of electrons within an octahedral crystal field, and finally the orbital-degenerate case with spin-orbit coupling.

1. Degenerate case

Starting with degenerate orbitals, we again apply the full cubic point group for the underlying symmetry analysis. The SC as well as the SK Hamiltonian are put into practice. The Slater-Condon form is employed for the two parametrizations $r = 0.625$ and 1.8. The resulting QP weights with respect to the Hubbard U are shown in Fig. 6. As in the three-orbital case, globally, the correlation strength increases with growing n for $J_H = 0$ and weakens for finite J_H. There is no clear trend concerning the size of the differences between the Hamiltonian forms, but those dependent strongly on filling and magnitude of the Hund's exchange. Characteristic features are nonetheless observable for all three local-interaction forms. The most prominent feature is again the Janus-face physics, which is most dominant for $n = 6$, but occurs also for $n = 7$ and with minor fingerprints also for $n = 8$. In comparison to the three-orbital case, the Janus-face signature especially for $n = 6$ appears more manifest. Again, $J_H/U = 0.7$ in the SC

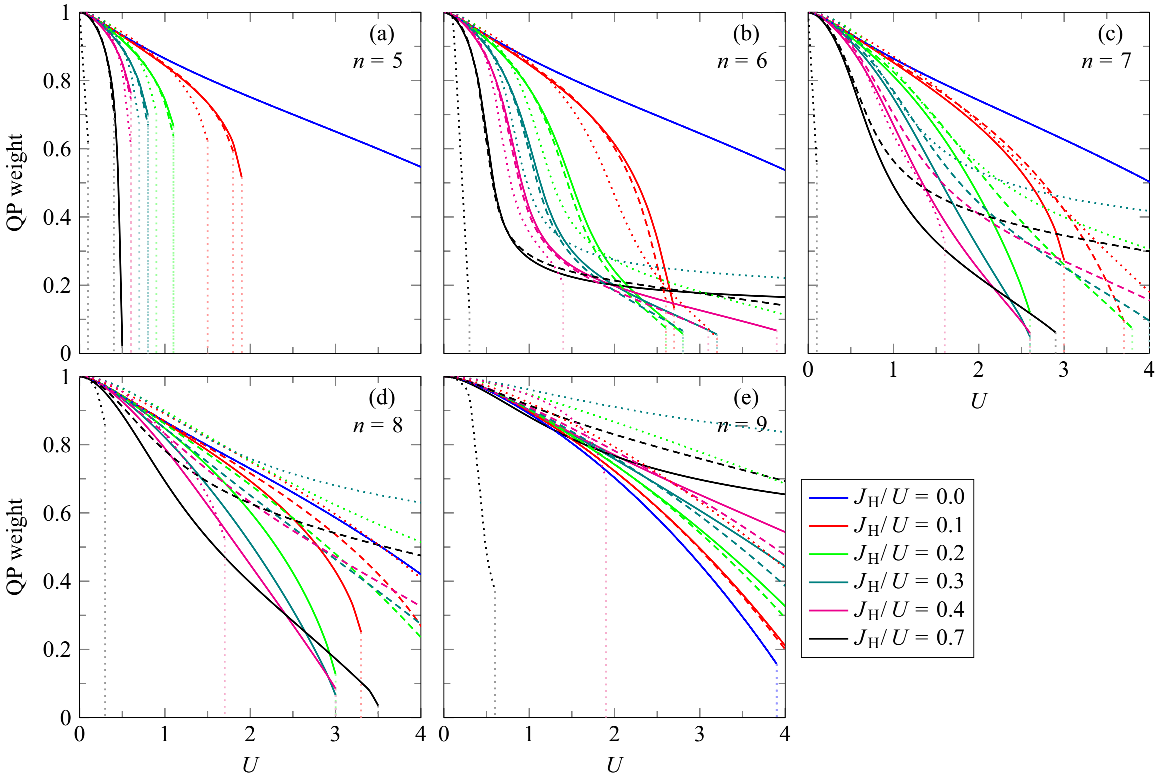

FIG. 6. Quasiparticle (QP) weight with respect to the Hubbard U for the degenerate five-orbital d-shell model at different fillings n and with varying J_H/U ratio. Solid lines: SC Hamiltonian with $r = 0.625$; dashed lines: SC Hamiltonian with $r = 1.8$; and dotted lines: SK Hamiltonian. Light dotted vertical lines are guides to the eyes for the critical U_c marking the Mott transition.

case with $r = 0.625$ and $J_H/U = 0.3$ in the SK display the strongest signature.

For the discussion of the slave-boson amplitudes, we restrict the data to the most adequate case of the SC($r = 0.625$) Hamiltonian. The amplitudes for the dominant multiplet states are shown in Fig. 7, with the explanation of the ϕ_Γ labeling in Table III. Nonsurprisingly, a one-dimensional A_1 spin sextet with five unpaired spins triggers the Mott transition at half-filling. On the other hand, the Janus-face phenomenology at $n = 6$ seems more intriguing than in the three-orbital case. Although again a seemingly concerted behavior of the dominant multiplets takes place, the higher seven-particle sector is not majorly involved. Instead, the named A_1 five-particle spin sextet and a six-particle $s = 2$ multiplet with T_2 symmetry are the key competitors, accompanied with another six-particle $s = 2$ multiplet of E symmetry. For smaller U, in particular the A_1- and E-symmetry states have similar weight, thus fluctuations between the five- and six-particle sectors occur via those symmetry channels. The energy separation between the relevant multiplets increases at larger fillings, giving rise to an increasingly decoupled behavior with less relevance of fluctuations.

2. *Cubic crystal-field splitting*

Degenerate p(-like) models may be adequate for some materials problems, e.g., for the threefold correlated t_{2g} electrons in SrVO$_3$ [67]. However, there is always a crystal-field splitting between the states of a d-shell atom on realistic lattices. Thus, we like to include an example application of our advanced RISB scheme to the simplest case, given by a five-orbital model with cubic crystal-field splitting, i.e., the term $\mathcal{H}^{(\mathrm{cf})}$ in the local Hamiltonian (21) becomes now nonzero. To facilitate the crystal field, a splitting $\Delta = 0.2$ between the $e_g = \{z^2, x^2 - y^2\}$ and the $t_{2g} = \{xz, yz, xy\}$ states is used, here explicitly reading as $\Delta_{e_g} = 3/5\Delta$ and $\Delta_{t_{2g}} = -2/5\Delta$ in view

TABLE III. Classification of dominant slave-boson amplitudes associated with local multiplets as plotted in Fig. 7 for the degenerate five-orbital model. See Table II for a detailed explanation of the symmetry labeling. All sums are normalized by a factor of $\sqrt{2s+1}$.

Γ	Symmetry	Nonzero
304	E: $\sum(4,2,\sigma,4,2,\{-2,0,2\})$	5
305	T_2: $\sum(4,1,\sigma,4,2,\{-2,-1,1,2\})$	6
568	A_1: $\sum(5,5/2,\sigma,5,0,0)$	1
776	E: $\sum(6,2,\sigma,4,2,\{-2,0,2\})$	5
777	T_2: $\sum(6,2,\sigma,4,2,\{-2,-1,1,2\})$	6
846	T_1: $\sum(7,3/2,\sigma,3,\{1,3\},\{-3,-1,0,1,3\})$	22
850	T_2: $\sum(7,3/2,\sigma,3,3,\{-3,-2,-1,1,2,3\})$	12
868	T_1: $\sum(8,1,\sigma,2,\{1,3\},\{-3,-1,1,3\})$	22
869	T_2: $\sum(8,1,\sigma,2,3,\{-3,-2,-1,1,2,3\})$	12
871	E: $\sum(9,1/2,\sigma,1,2,\{-2,0,2\})$	5
872	E: $\sum(9,1/2,\sigma,1,2,\{-2,-1,1,2\})$	6
873	A_1: (10,0,0,0,0,0)	1

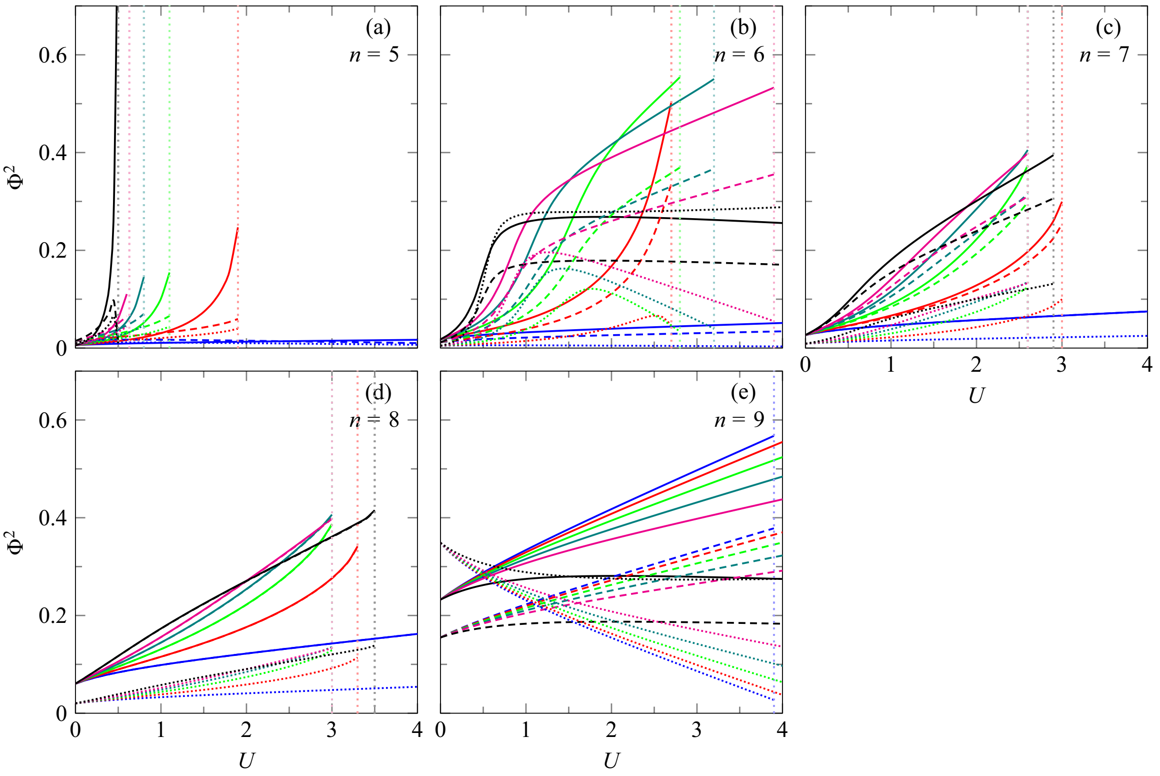

FIG. 7. Slave-boson amplitudes of dominant multiplets in the degenerate five-orbital model at different filling n using the SC Hamiltonian. Colors mark different J_{H}/U, with the coding as in Fig. 6. (a) solid line: ϕ_{568}; dashed line: ϕ_{305}; dotted line: ϕ_{304}. (b) Solid line: ϕ_{777}; dashed line: ϕ_{776}; dotted line: ϕ_{568}. (c) Solid line: ϕ_{850}; dashed line: ϕ_{846}; dotted line: ϕ_{851}. (d) Solid line: ϕ_{869}; dashed line: ϕ_{868}; dotted line: ϕ_{872}. (e) Solid line: ϕ_{872}; dashed line: ϕ_{871}; dotted line: ϕ_{873}. The symmetry/quantum number classification of the respective amplitudes is given in Table III.

of Eq. (22) (cf. Fig. 1). This resembles a simplistic model for an oxide perovskite where the key transition-metal site is located on a simple-cubic lattice and explicit oxygen degrees of freedom in octahedral position are integrated out. Note that the hoppings for the different orbitals within the d shell are here kept identical.

Albeit the problem of competing high- and low-spin states in five-orbital manifolds with crystal field is a prominent one, in our basic application we do not investigate such physics. The present crystal-field size is rather small compared to the bandwidth as well as the local Coulomb interactions. Hence, the theoretical treatment does not result in obvious low-spin states, and furthermore an explicit effort to reveal high-to-low-spin transitions is not undertaken.

Figure 8 exhibits the (e_g,t_{2g}) QP weight for different fillings and varying J_{H}/U ratio, while Fig. 9 displays the associated orbital fillings. Due to the chosen crystal-field splitting, the t_{2g} states are lower in energy than the e_g ones and therefore have larger occupation. At half-filling $n = 5$, the correlation strength of the two orbital sectors is nearly degenerate and increases with growing J_{H}/U. The filling difference $n_{t_{2g}} - n_{e_g}$ tends to grow with rising U, but then decreases again close to the Mott transition. For fixed U, a larger Hund's exchange reduces the filling difference since J_{H} favors orbital balancing and is a natural opponent of the crystal-field splitting. As expected, away from half-filling the correlation and filling scenario is more sophisticated. For the electron-doped $n = 6$ case, the Hund's physics results in a manifest interplay of the Janus-face behavior with orbital-selective mechanisms. The less-filled e_g states are close to half-filling and become more strongly correlated than t_{2g}. For $J_{\mathrm{H}}/U > 0.1$, while both orbital sectors develop Janus-face signature, the e_g orbitals become localized at larger U with the t_{2g} orbitals still metallic [54]. The localization of the t_{2g} states takes then place at even larger U. Within the orbital-selective e_g-localized sector, the occupation is fixed to half-filled orbitals. Further electron doping leads to a quick vanishing of the orbital-selective behavior. For $n = 7$ it only occurs in a small-U window for the extreme case $J_{\mathrm{H}}/U = 0.7$. For $n = 7,8$ the (e_g,t_{2g}) sectors, though with different QP weight, enter the Mott-insulating regime at the same critical interaction strength via a first-order transition.

Note that there is an obvious breaking of particle-hole symmetry with crystal-field splitting: whereas an additional electron most likely enters the lower-lying crystal-field level, an additional hole usually favors the higher-lying one. Thus, in the hole-doped case of $n = 4$, the t_{2g} states are now close to half-filling, whereas the e_g ones are closer to quarter-filling. This leads to an inverse orbital-selective behavior in comparison to $n = 6$. Namely, the t_{2g} orbitals become first localized and afterwards the e_g orbitals at larger interaction strength. Because of the different size of the orbital sectors, the $Z(U)$ curves for $n = 4,6$ differ not only by an interchange of e_g against t_{2g}.

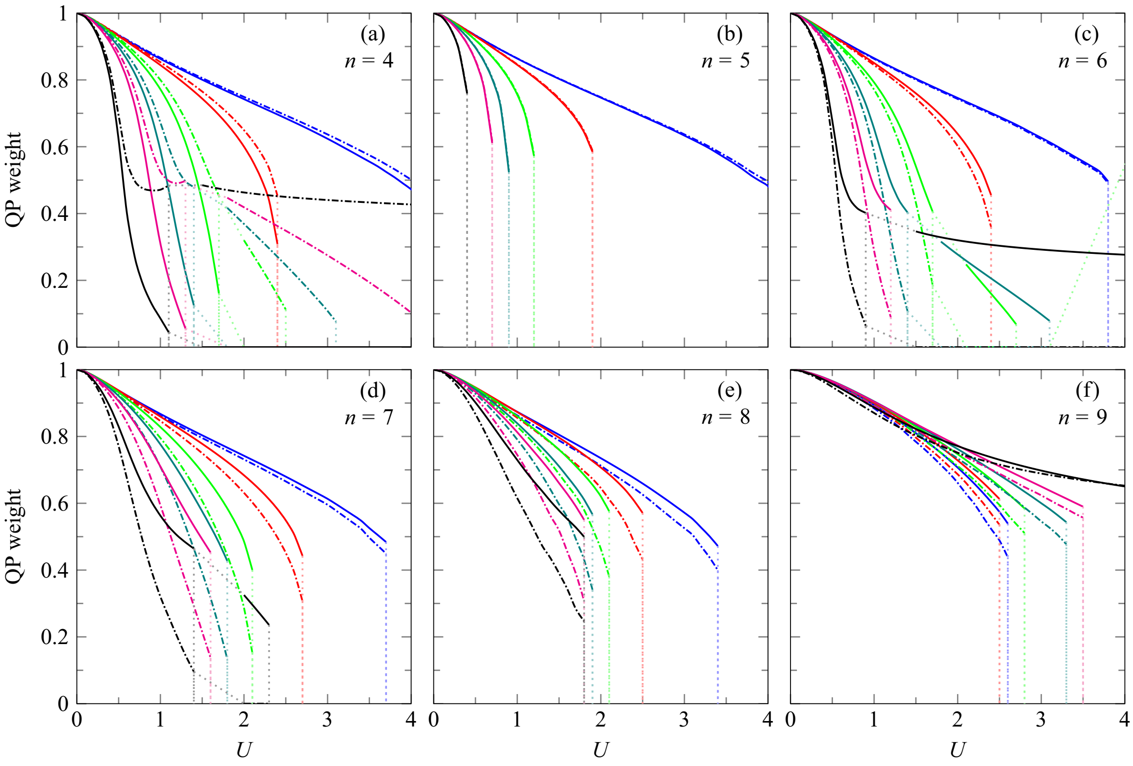

FIG. 8. Quasiparticle weight with respect to the Hubbard U for the five-orbital d-shell model with cubic crystal field, at different fillings n and with varying J_{H}/U ratio. The SC Hamiltonian with $r = 0.625$ is employed. Solid lines: t_{2g} states; dashed lines: e_g states. Colors mark different J_{H}/U, with the coding as in Fig. 6. Light dotted vertical lines are guides to the eyes for the critical U_c marking the Mott transition.

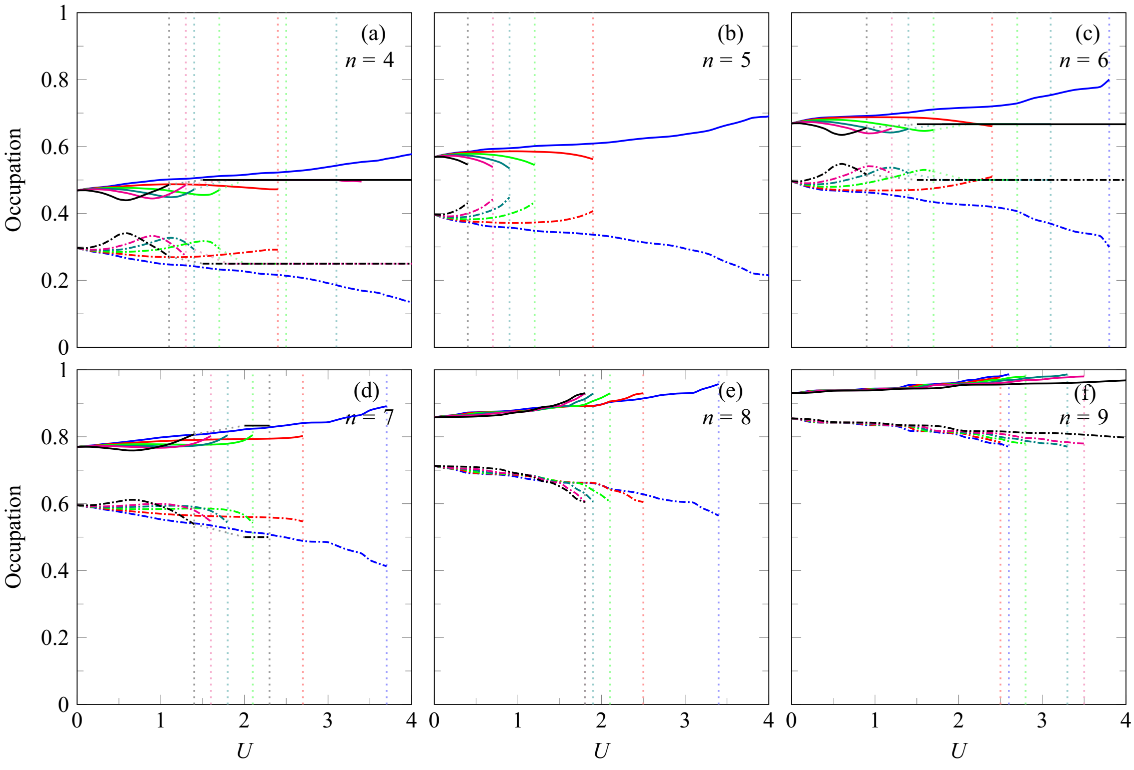

FIG. 9. Occupation of the e_g (solid line) and the t_{2g} (dashed line) orbitals with respect to the Hubbard U for the five-orbital d-shell model with cubic crystal field, at different fillings n and with varying J_{H}/U ratio. The data are given per orbital and per spin, i.e., the total e_g (t_{2g}) occupation is obtained by multiplication with 4 (6). The SC Hamiltonian with $r = 0.625$ is employed. Light dotted vertical lines are guides to the eyes for the critical U_c marking the Mott transition.

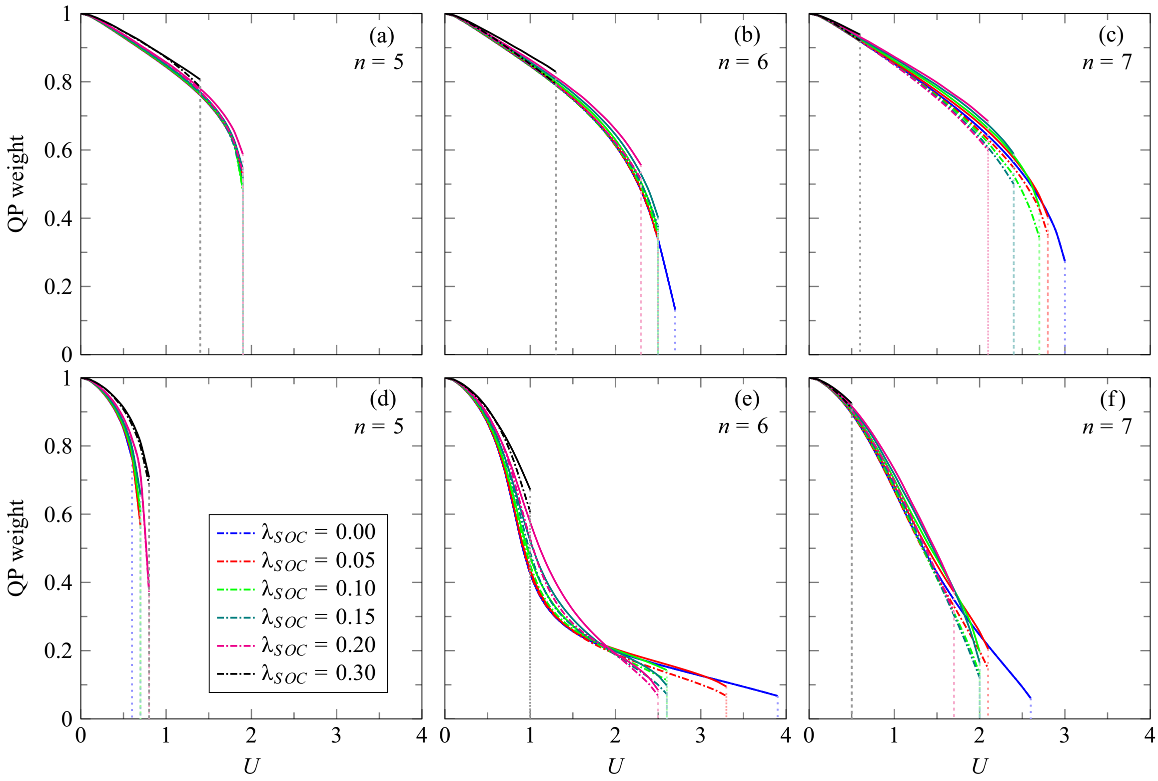

FIG. 10. Quasiparticle weight with respect to the Hubbard U for the degenerate five-orbital d-shell model with spin-orbit coupling, at different fillings n and two different regimes for the Hund's exchange: (a)–(c) $J_{\mathrm{H}}/U = 0.1$ and (d)–(f) $J_{\mathrm{H}}/U = 0.4$. The SC Hamiltonian with $r = 0.625$ is employed. Full lines: $j = \frac{3}{2}$; dashed lines: $j = \frac{5}{2}$. Light dotted vertical lines are guides to the eyes for the critical U_c marking the metal-insulator transition.

3. Spin-orbit coupling

We conclude the model applications by providing results for the degenerate five-orbital model with finite spin-orbit coupling. The interplay between electron correlations and SOC has become of seminal interest in the study of strongly correlated materials [26,28,68–71]. Especially for certain 4d and 5d transition-metal compounds, processes based on interweaved Mott and SOC physics may lead to intriguing phenomena. But, also for specific correlated 3d compounds such as, e.g., the iron pnictides and chalcogenides [72], the impact of the spin-orbit interaction is heavily discussed.

Here, we again provide only a glimpse on this phenomenology, mainly to illustrate the power and potential of the advanced RISB scheme to tackle this issue. Albeit the interplay of crystal-field splitting and spin-orbit coupling is often a relevant physics in materials, we restrict the basic discussion here to the degenerate five-orbital model on a cubic lattice. The Slater-Condon Hamiltonian (with $r = 0.625$) for the local interaction is utilized and two distinct ratios J_{H}/U are employed with rising spin-orbit-interaction parameter λ_{soc}. Namely, we study the cases $J_{\mathrm{H}}/U = 0.1$ and $J_{\mathrm{H}}/U = 0.4$. The chosen λ_{SOC} values put us in the regime of strong spin-orbit coupling, e.g., as applicable for iridates [73]. Basically, the additional interaction gives rise to states in the five-orbital manifold, given by the quantum number $j = l \pm 1/2$. For the case of a complete d shell with $l = 2$, the j states split into two manifolds: a threefold-degenerate group with $j = \frac{5}{2}$ and a twofold-degenerate group with $j = \frac{3}{2}$. Hence, as in the former case of a (e_g, t_{2g}) crystal field, a splitting of the physical quantities into two sectors is expected. Since we keep λ_{SOC} positive, the $j = \frac{3}{2}$ manifold lies lower than the $j = \frac{5}{2}$ one.

Figure 10 displays the quasiparticle weight Z for different fillings n. Indeed, one may observe the grouping into the both $j = \frac{5}{2}, \frac{3}{2}$ sectors, respectively. From Z, a finite spin-orbit coupling leads to a further lowering of the critical Hubbard U, i.e., increases the correlation strength for fixed Coulomb-interaction parameters. With growing deviation from half-filling, this effect also becomes stronger in relative size. Most interesting is the case of $n = 6$ and sizable J_{H}/U, i.e., the setting that results in the Janus-face regime. There, a rising spin-orbit coupling weakens the Janus-face signature, with a final disappearance at $\lambda_{\mathrm{SOC}} = 0.3$. Note that overall for every filling and interaction, there is no "orbital-selective" Mott transition taking place. Contrary to the crystal-field case, both j sectors become insulating at the identical interaction strength. Still, the fillings in the two sectors are respectively rather different (see Fig. 11). The effective spin-orbit splitting results in a stronger-filled $j = \frac{3}{2}$ manifold, which for rising U and sizable λ_{SOC} rather quickly becomes fully occupied. Only in the original Janus-face regime, the j polarization may be contained for not-too large λ_{SOC} within a larger regime of U values.

C. Realistic application: Iron chalcogenides

In the final application, we tackle a realistic problem and show that the advanced RISB scheme allied with DFT may

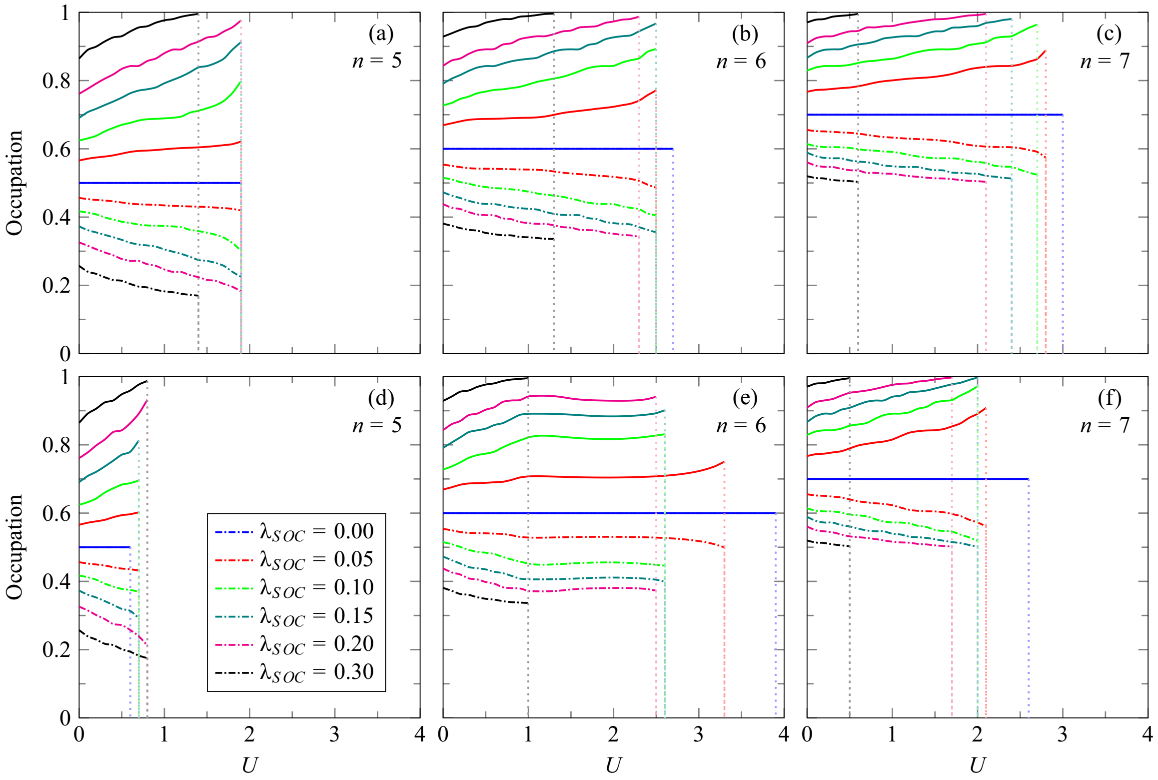

FIG. 11. Occupation with respect to the Hubbard U in the degenerate five-orbital d-shell model with spin-orbit coupling, at different fillings n and two different regimes for the Hund's exchange: (a)–(c) $J_{\mathrm{H}}/U = 0.1$ and (d)–(f) $J_{\mathrm{H}}/U = 0.4$. The SC Hamiltonian with $r = 0.625$ is employed. Full lines: $j = \frac{3}{2}$; dashed lines: $j = \frac{5}{2}$. Light dotted vertical lines are guides to the eyes for the critical U_c marking the metal-insulator transition.

serve as a versatile theoretical tool to analyze intricate correlated materials. Documenting a materials case for the reported technical advancements is the present main concern. The prominent iron chalcogenides FeSe and FeTe as compounds with seemingly important Hund's physics are adequate materials examples [74–77] in line with the previous discussions in the model context. Note that combinations of Gutzwiller techniques and DFT have been applied to the problem of Fe pnictides and chalcogenides in previous works [54,78,79].

Figure 12(a) depicts the symmetry-identical α-phase crystal structure of tetragonal kind (space group $P4/nmm$) of the two compounds. Iron square lattices with lattice constant a, having Se, Te up and below the square center in a distance h, are stacked along the c axis with distance c. Based on the available experimental data [80,81], we employed $a^{(\mathrm{FeSe})} = 3.77$ Å, $a^{(\mathrm{FeTe})} = 3.82$ Å; $c^{(\mathrm{FeSe})} = 5.52$ Å, $c^{(\mathrm{FeTe})} = 6.29$ Å and $h^{(\mathrm{FeSe})} = 1.47$ Å, $h^{(\mathrm{FeTe})} = 1.76$ Å. Hence, as expected, the FeTe compound has increased lattice parameters compared to FeSe, most significantly a more elongated c-axis parameter. The nominal filling of the Fe 3d shell amounts to $n = 6$ electrons, i.e., as also learned from the previous model results, the systems are good candidates for manifest Hund's physics. There are various theoretical assessments of the local Coulomb integrals for iron pnictides and chalcogenides, e.g., [82,83]. Therefrom it is agreed that a value for the Hubbard interaction of $U = 4.0$ eV and a value for the Hund's exchange of $J_{\mathrm{H}} = 0.8$ eV, i.e., $J_{\mathrm{H}}/U = 0.2$, are proper choices. In order to study the relevance of J_{H}, we here take again U as a parameter and allow for two different ratios between the Hubbard interaction and the Hund's exchange, namely, $J_{\mathrm{H}}/U = 0.15$ and $J_{\mathrm{H}}/U = 0.224$.

1. DFT characterization

Let us first report the results within density functional theory (DFT) using the generalized-gradient approximation (GGA) based on the Perdew-Burke-Ernzerhof exchange-correlation functional [84]. Original DFT results for FeSe and FeTe have been presented by Subedi *et al.* [85]. Here, we construct a Wannier-type characterization of the DFT(GGA) electronic structure based on projected-local orbitals [60]. The Fe 3d shell is split by crystal field, leading to onsite levels $\varepsilon_m = \{z^2, x^2 - y^2, xz, yz, xy\}$. Those read as $\varepsilon_m^{(\mathrm{FeSe})} = \{-235, -459, 100, 100, 156\}$ meV and $\varepsilon_m^{(\mathrm{FeTe})} = \{-200, -285, 177, 177, 138\}$ meV. Thus, although the internal (e_g, t_{2g}) degeneracy is mostly lifted within the tetragonal symmetry, the e_g manifold is energetically favored against t_{2g}. This yields also a stronger filling of the e_g states. The orbital-resolved DFT fillings (in the same order as the crystal-field levels) read as $n_m^{(\mathrm{FeSe})} = \{1.50, 1.15, 1.13, 1.13, 1.05\}$ and $n_m^{(\mathrm{FeTe})} = \{1.48, 1.11, 1.15, 1.15, 1.10\}$. Note that the crystal-field level of the x^2-y^2 orbital is lower than the z^2 one. But, due to the wider bimodal local density of states (lDOS) of the former [cf. Fig. 12(b)], related to the major contribution to the in-plane bonding, the electron occupation is highest in the z^2 state. Both compounds have a seemingly very similar DFT electronic

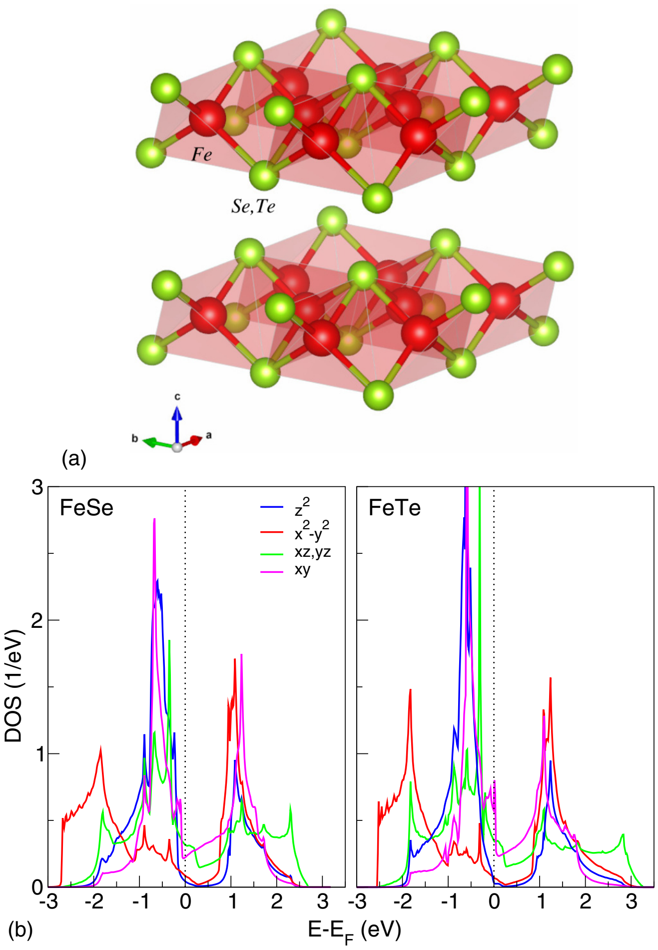

FIG. 12. (a) $P4/nmm$ crystal structure and (b) DFT orbital-resolved local density of states (lDOS) of FeSe and FeTe.

structure, e.g., the dominant in-plane bonding between x^2-y^2 orbitals is mediated by a nearest-neighbor hopping amplitude of $t_{x^2\text{-}y^2} = -438$ meV for FeSe and of $t_{x^2\text{-}y^2} = -433$ meV for FeTe. But, some differences are observable. FeTe has a slightly larger bandwidth, i.e., 5.6 eV compared to the 5.3 eV of FeSe. Furthermore, FeTe has a sharper z^2 as well as xz,yz lDOS and higher density of states at the Fermi level compared to FeSe. In comparison to the previous model studies, an effective Hubbard interaction normalized to the half-bandwidth reads as $U_{\text{eff}} \sim 4.0/2.7 \sim 1.5$.

2. RISB quasiparticle weights and orbital occupations

We first employ the DFT Kohn-Sham Hamiltonian obtained within the projected-local-orbital formalism in the "one-shot" or "post-processing" combinational scheme with RISB, similar to the previous approaches by Schickling *et al.* [79] and Lanatà *et al.* [54]. To facilitate this, the proper symmetry relations invoked by the tetragonal point group are implemented and utilized.

Before discussing the concrete results, it is important to realize the differences of the present realistic problem compared to the model five-orbital problem with crystal field from Sec. VI B 2. First, the reduced tetragonal symmetry lifts the degeneracy within the e_g and t_{2g} subshells, and the crystal-field splitting is now also active between these nondegenerate levels. Second, the intraorbital hopping becomes orbital dependent and is not bound to the nearest-neighbor term as in the model case. Third, there are in addition also interorbital hopping terms from short to longer range included in the Kohn-Sham Hamiltonian.

Figure 13 shows the resulting orbital-dependent quasiparticle weights as well as occupation with rising Hubbard U. From the QP weights, the FeSe compound seems slightly more correlated than FeTe, providing also a lower critical U_c for the theoretical Mott transition. The least-filled xy orbital is most strongly correlated as it resides closest to half-filling, similar as the scenario in the model case. For the case of larger $J_H/U = 0.224$, which is closer to the assumed realistic interaction, indeed the Janus-face signature sets in, and is most pronounced for xy. The iron chalcogenides are hence truly a clear case for dominant Hund's physics. But, note that no explicit orbital-selective behavior is observed, in contrast to the model case with crystal field. This is probably due to the longer-range and intraorbital hoppings that lead to a stronger entanglement of the orbital correlations. Interestingly, there is a crossover in the z^2 vs x^2-y^2 occupations with rising U. For larger U closer to the Mott transition, the x^2-y^2 orbital gains more electrons. This filling-hierarchy change happens for the larger J_H/U ratio at smaller U, close to the expected value of $U = 4$ eV. For completeness, we included the FeSe data for the Slater-Condon Hamiltonian with $r = 1.8$ as well as the Slater-Kanamori Hamiltonian. While the former does not yield significant changes, the use of the latter simplified Hamiltonian form results in somewhat stronger correlations for intermediate U, but shifts the theoretical Mott transition to larger interaction strengths.

Finally, we incorporated charge self-consistent DFT+RISB results for Z and the orbital occupations at $U = 1$ and 6 eV. The effect of charge self-consistency for the QP weight is generally minor, qualitatively heading to a slight correlation-strength increase. But, there are changes for the orbital occupations at larger U. Namely, the mentioned crossover in the filling hierarchy within the one-shot calculations tends to be shifted to larger U or is even absent in the CSC treatment. Thus, the orbital occupations especially in the e_g states of the iron chalcogenides appear to be sensitive to the many-body charge-density handling. Note that we do not touch on the prominent issue of nematicity [86] in the present context. Since the tetragonal symmetry is hard cored here and spin-orbit effects are neglected in this realistic example, such anisotropic effects are excluded. Future studies lifting those restrictions may enable results on this specific physics.

VII. SUMMARY

We here documented a rigorous implementation of the mean-field version of the rotational-invariant slave-boson (RISB) approach in terms of an efficient symmetry-adapted handling of multiorbital degrees of freedom. The point-group symmetry of the underlying lattice is used to reduce by general means the number of relevant slave-boson amplitudes. Complete generality in the form of the local Hamiltonian ensures access to demanding interacting lattice problems. Spin-orbit coupling is naturally included in the symmetry-faithful for-

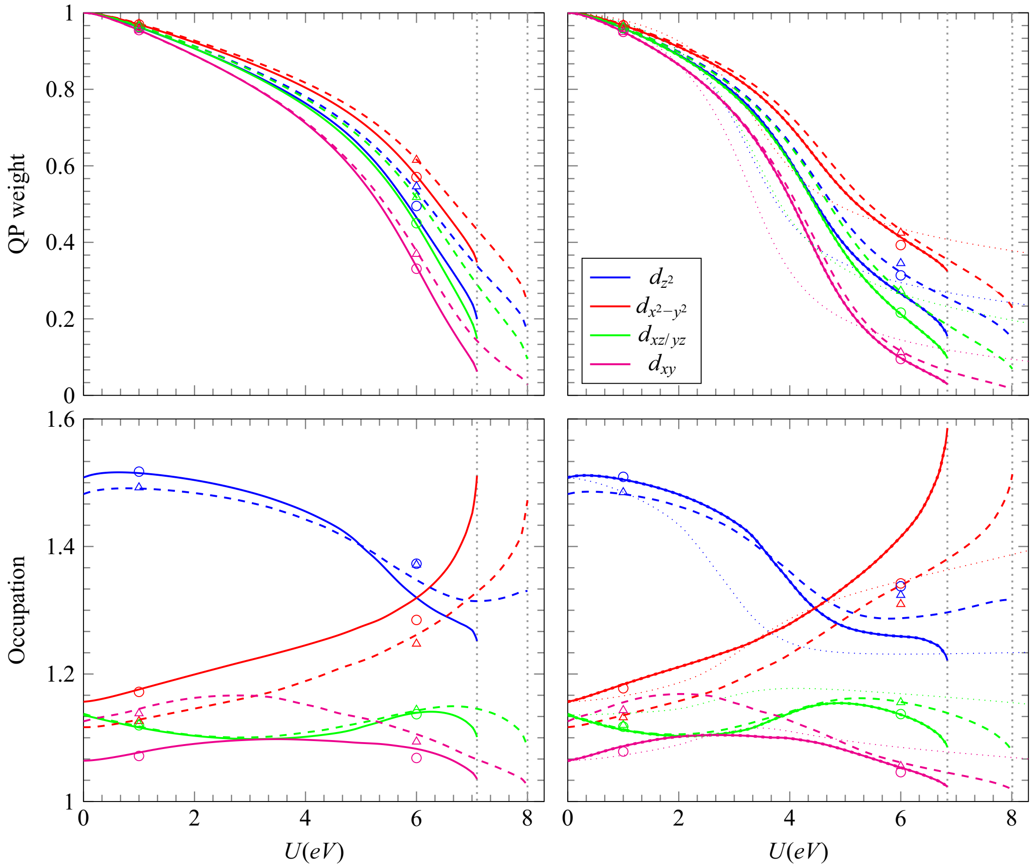

FIG. 13. Orbital-resolved quasiparticle weight (top) and occupation (bottom) for FeSe (solid lines) and FeTe (dashed lines). For the interacting part, the SC Hamiltonian with $r = 0.625$ is used. Results from charge self-consistent calculations are given by by circles (triangles) for FeSe (FeTe). Left panel: $J_{\mathrm{H}}/U = 0.150$; right panel: $J_{\mathrm{H}}/U = 0.224$. For comparison, the right panel additionally contains FeSe results for the SC Hamiltonian with $r = 1.8$ (thick dashed lines, mostly on top of the $r = 0.625$ curves) and for the SK Hamiltonian (light dotted lines).

malism via the introduction of double-group representations. In this work, the degree of complexity is limited to cubic and tetragonal symmetries for up to five local orbitals, suitable for generic d-shell studies. However, a further advancement of the present scheme to other (low-)symmetry cases is straightforward and with the present computing power, seven-orbital problems, i.e., treating a full interacting f shell, are in principle within the performance capabilities. The advanced RISB framework is implemented such as to be applied to model Hamiltonians, to one-shot combinations with DFT, or within a full charge self-consistent DFT+RISB methodology.

Selected applications within the prominent research field of Hund's physics have been presented, however, without providing an in-depth survey of the encountered physics. The Hund's physics with its highlighting influence of the Hund's exchange J_{H} in the presence of a finite Hubbard U came here across for three- and five-orbital models, as well as in the realistic context of the FeSe and FeTe compounds. The emergence of the Janus-face signature and its interplay with orbital-selective physics in the presence of a crystal field were reported for the model cases. Moreover, we showed the weakening of this hallmark signature with finite spin-orbit interaction. The reliability of the method also for true materials problems was proven by verifying FeSe and FeTe as the known Hund's materials. Thereby, advanced RISB is capable of dealing with the subtle differences in the electronic structure. We showed that the e_g polarizations of z^2 and x^2-y^2 kind in these iron chalcogenides are prone to an orbital crossover, which might be relevant for fluctuation-driven processes in the given materials.

ACKNOWLEDGMENT

Computations were performed at the North-German Supercomputing Alliance (HLRN) under Grant No. hhp00035.

APPENDIX A: COMPUTATION OF THE RENORMALIZATION MATRIX

The renormalization matrix **R** may be computed in the multiorbital framework as follows. Equation (37) provides the standard form for the renormalization matrix, reading as

$$R^*_{\alpha\beta} = \sum_{\gamma} T^*_{\alpha\gamma} w_{\gamma\beta}. \tag{A1}$$

The matrix **T** can be written as

$$T^*_{\alpha\gamma} = \mathrm{Tr}(\phi^\dagger f^\dagger_\alpha \phi c_\gamma) \tag{A2}$$

since

$$\begin{aligned}\mathrm{Tr}(\phi^\dagger f_\alpha^\dagger \phi c_\gamma) &= \sum_{AB,CD} \phi^\dagger_{AB}(f_\alpha^\dagger)_{BC}\phi_{CD}(c_\gamma)_{DA}\\ &= \sum_{AB,CD} \phi^*_{BA}(f_\alpha^\dagger)_{BC}\phi_{CD}(c_\gamma)_{DA}\\ &= \sum_{AB,CD} \langle B|f_\alpha^\dagger|C\rangle\langle D|c_\gamma|A\rangle\phi^*_{BA}\phi_{CD}\\ &= \sum_{AB,CD} \langle B|f_\alpha^\dagger|C\rangle\langle A|c_\gamma^\dagger|D\rangle^*\phi^*_{BA}\phi_{CD}. \end{aligned} \tag{A3}$$

As the element $\langle A|c_\gamma^\dagger|D\rangle$ is a real number when using the Fock basis, this form can also be written in the following way:

$$\mathrm{Tr}(\phi^\dagger f_\alpha^\dagger \phi c_\gamma) = \sum_{AB,nm} \langle A|f_\alpha^\dagger|B\rangle\langle n|c_\gamma^\dagger|m\rangle^*\phi^*_{An}\phi_{Bm}, \tag{A4}$$

when changing notation, i.e., $B \to A$, $C \to B$, $A \to n$, $D \to m$. Therewith, the final expression coincides with the formula for the renormalization matrix in the original RISB paper [17].

APPENDIX B: GENERATION OF BASIS MATRICES

(1) We start with a representation Θ of the point group G on the local many-body states (i.e., the adapted basis) $\mathcal{A}$. It is constructed by taking the Euler (angular-momentum) representation of every group element and repeating it for all other combinations of quantum numbers other than the total angular momentum. This creates off-diagonal matrices, which by construction contain the point-group representation multiple repeated times. The number of repetitions $\mathcal{R}$ can be obtained from the vector product of the character vector of the representation Θ $[\chi(\Theta)]$ and the character vector of an irreducible representation $\chi(\Theta^\alpha)$, normalized to the number of group elements n_G:

$$r = \frac{1}{n_G}\chi(\Theta)\,\chi(\Theta^\alpha). \tag{B1}$$

(2) Then, Casimir-type operators C_i are built, one for every equivalence class, by summing up all elements of one equivalence class in the above representation, via

$$0 = [C_i, g] \quad \forall i, g. \tag{B2}$$

They commutate with all elements g of the group and with each other. The commutating set of C_i operators can be simultaneously diagonalized. The emerging basis block diagonalizes all elements of the group in blocks of dimension of the irreducible representation times its repetitions, i.e., $\dim(\Theta^\alpha)\,\mathcal{R}$.

(3) To find a basis $\mathcal{K}$ that diagonalizes all elements of the group, one has to perform a Koster-phase fixing [53] to separate repeated irreducible representations from each other by means of an irreducible representation Θ^α of the same point group.

(4) Now, identity matrices of the dimension of the irreducible representation are set up, according to Schur's lemma commutating with all elements of the group (up to a complex factor, which will play the role of the variational parameter in our context). All basis matrices for the actual irreducible representation that commutate with all group elements in basis $\mathcal{K}$ are now identified by taking each and every summand of the (off-diagonal) direct sum of the identity matrices separately, according to the number of repetitions, which amounts to $n_{\tilde{\phi}}(\Theta^\alpha) = \mathcal{R}^2$ different matrices.

(5) Rotating these identity matrices back to $\mathcal{A}$ results in the desired basis matrices.

[1] M. C. Gutzwiller, Phys. Rev. Lett. **10**, 159 (1963).
[2] J. Bünemann and F. Gebhard, Phys. Rev. B **76**, 193104 (2007).
[3] J. Bünemann, W. Weber, and F. Gebhard, Phys. Rev. B **57**, 6896 (1998).
[4] L. Huang, L. Du, and X. Dai, Phys. Rev. B **86**, 035150 (2012).
[5] N. Lanatà, H. U. R. Strand, X. Dai, and B. Hellsing, Phys. Rev. B **85**, 035133 (2012).
[6] S. E. Barnes, J. Phys. F: Met. Phys. **6**, 1375 (1976).
[7] P. Coleman, Phys. Rev. B **28**, 5255 (1983).
[8] N. Read and D. Newns, J. Phys. C: Solid State Phys. **16**, 3273 (1983).
[9] G. Kotliar and A. E. Ruckenstein, Phys. Rev. Lett. **57**, 1362 (1986).
[10] D. P. Arovas and A. Auerbach, Phys. Rev. B **38**, 316 (1988).
[11] G. Kotliar and J. Liu, Phys. Rev. B **38**, 5142(R) (1988).
[12] T. Li, P. Wölfle, and P. J. Hirschfeld, Phys. Rev. B **40**, 6817 (1989).
[13] H. Hasegawa, J. Phys. Soc. Jpn. **66**, 1391 (1997).
[14] R. Frésard and G. Kotliar, Phys. Rev. B **56**, 12909 (1997).
[15] S. Florens and A. Georges, Phys. Rev. B **70**, 035114 (2004).
[16] L. de' Medici, A. Georges, and S. Biermann, Phys. Rev. B **72**, 205124 (2005).
[17] F. Lechermann, A. Georges, G. Kotliar, and O. Parcollet, Phys. Rev. B **76**, 155102 (2007).
[18] A. Isidori and M. Capone, Phys. Rev. B **80**, 115120 (2009).
[19] J. Bünemann, Phys. Status Solidi B **248**, 203 (2011).
[20] A. B. Georgescu and S. Ismail-Beigi, Phys. Rev. B **92**, 235117 (2015).
[21] J. I. Facio, V. Vildosola, D. J. García, and P. S. Cornaglia, Phys. Rev. B **95**, 085119 (2017).
[22] M. Raczkowski, R. Frésard, and A. M. Oleś, Phys. Rev. B **73**, 174525 (2006).
[23] F. Lechermann, Phys. Rev. Lett. **102**, 046403 (2009).
[24] M. Ferrero, P. S. Cornaglia, L. De Leo, O. Parcollet, G. Kotliar, and A. Georges, Phys. Rev. B **80**, 064501 (2009).
[25] I. I. Mazin, H. O. Jeschke, F. Lechermann, H. Lee, M. Fink, R. Thomale, and R. Valentí, Nat. Commun. **5**, 4261 (2014).
[26] M. Behrmann, C. Piefke, and F. Lechermann, Phys. Rev. B **86**, 045130 (2012).
[27] S. Schuwalow, C. Piefke, and F. Lechermann, Phys. Rev. B **85**, 205132 (2012).
[28] A. Hampel, C. Piefke, and F. Lechermann, Phys. Rev. B **92**, 085141 (2015).
[29] M. Behrmann and F. Lechermann, Phys. Rev. B **91**, 075110 (2015).
[30] M. Behrmann and F. Lechermann, Phys. Rev. B **92**, 125148 (2015).
[31] M. Schiró and M. Fabrizio, Phys. Rev. Lett. **105**, 076401 (2010).

[32] M. Behrmann, M. Fabrizio, and F. Lechermann, Phys. Rev. B **88**, 035116 (2013).
[33] M. Behrmann, A. I. Lichtenstein, M. I. Katsnelson, and F. Lechermann, Phys. Rev. B **94**, 165120 (2016).
[34] P. Werner, E. Gull, M. Troyer, and A. J. Millis, Phys. Rev. Lett. **101**, 166405 (2008).
[35] K. Haule and G. Kotliar, New J. Phys. **11**, 025021 (2009).
[36] L. de' Medici, J. Mravlje, and A. Georges, Phys. Rev. Lett. **107**, 256401 (2011).
[37] A. Georges, L. de' Medici, and J. Mravlje, Annu. Rev. Condens. Matter Phys. **4**, 137 (2013).
[38] In order not to overburden the notation, we do not mark quantum operators explicitly. The difference to c numbers should be obvious from the context, or is mentioned explicitly when needed.
[39] One-dimensional physics is in principle also accessible via RISB by invoking a cluster description (see Sec. II B). Yet, within the scope of this work, we are not discussing such variations of the method.
[40] P. Wölfle, J. Low Temp. Phys **99**, 625 (1995).
[41] C. Nayak, Phys. Rev. Lett. **85**, 178 (2000).
[42] P. A. Lee, N. Nagaosa, and X.-G. Wen, Rev. Mod. Phys. **78**, 17 (2006).
[43] R. Frésard and T. Kopp, Ann. Phys. (Berlin) **524**, 175 (2012).
[44] N. Lanatà, Y. Yao, X. Deng, V. Dobrosavljević, and G. Kotliar, Phys. Rev. Lett. **118**, 126401 (2017).
[45] A. Georges, G. Kotliar, W. Krauth, and M. J. Rozenberg, Rev. Mod. Phys. **68**, 13 (1996).
[46] G. Kotliar and D. Vollhardt, Phys. Today **57**(3), 53 (2004).
[47] R. Raimondi and C. Castellani, Phys. Rev. B **48**, 11453(R) (1993).
[48] W. Zimmermann, R. Frésard, and P. Wölfle, Phys. Rev. B **56**, 10097 (1997).
[49] T. Maier, M. Jarrell, T. Pruschke, and M. H. Hettler, Rev. Mod. Phys. **77**, 1027 (2005).
[50] G. W. F. Drake, *Springer Handbook of Atomic, Molecular, and Optical Physics* (Springer, New York, 2006).
[51] Z. Rudzikas, *Theoretical Atomic Spectroscopy* (Cambridge University Press, Cambridge, 2007).
[52] The trace operation “Tr” is throughout this work generally understood as the summation of the diagonal elements of the involved objects.
[53] G. F. Koster, Phys. Rev. **109**, 227 (1958).
[54] N. Lanatà, H. U. R. Strand, G. Giovannetti, B. Hellsing, L. de' Medici, and M. Capone, Phys. Rev. B **87**, 045122 (2013).
[55] N. Lanatà, Y. Yao, C.-Z. Wang, K.-M. Ho, and G. Kotliar, Phys. Rev. X **5**, 011008 (2015).
[56] In the following, the indices i,j denote different basis matrices and should not be confused with lattice-site indices.
[57] A. Hjørungnes, *Complex-Valued Matrix Derivatives* (Cambridge University Press, Cambridge, 2011).
[58] J. R. Dennis Jr. and R. B. Schnabel, *Numerical Methods for Unconstraint Optimization and Nonlinear Equations* (Society for Industrial and Applied Mathematics, Philadelphia, 1996).
[59] B. Meyer, C. Elsässer, F. Lechermann, and M. Fähnle, FORTRAN 90 Program for Mixed-Basis-Pseudopotential Calculations for Crystals, Max-Planck-Institut für Metallforschung, Stuttgart (unpublished).
[60] B. Amadon, F. Lechermann, A. Georges, F. Jollet, T. O. Wehling, and A. I. Lichtenstein, Phys. Rev. B **77**, 205112 (2008).
[61] D. Grieger, C. Piefke, O. E. Peil, and F. Lechermann, Phys. Rev. B **86**, 155121 (2012).
[62] V. I. Anisimov, I. V. Solovyev, M. A. Korotin, M. T. Czyżyk, and G. A. Sawatzky, Phys. Rev. B **48**, 16929 (1993).
[63] G.-T. Wang, X. Dai, and Z. Fang, Phys. Rev. Lett. **101**, 066403 (2008).
[64] G. Borghi, M. Fabrizio, and E. Tosatti, Phys. Rev. B **90**, 125102 (2014).
[65] K. M. Ho, J. Schmalian, and C. Z. Wang, Phys. Rev. B **77**, 073101 (2008).
[66] R. Frésard and M. Lamboley, J. Low Temp. Phys. **126**, 1091 (2002).
[67] E. Pavarini, A. Yamasaki, J. Nuss, and O. K. Andersen, New J. Phys. **7**, 188 (2005).
[68] G. Jackeli and G. Khaliullin, Phys. Rev. Lett. **102**, 017205 (2009).
[69] D. Pesin and L. Balents, Nat. Phys. **6**, 376 (2010).
[70] H. Watanabe, T. Shirakawa, and S. Yunoki, Phys. Rev. Lett. **105**, 216410 (2010).
[71] C. Martins, M. Aichhorn, L. Vaugier, and S. Biermann, Phys. Rev. Lett. **107**, 266404 (2011).
[72] S. V. Borisenko, D. V. Evtushinsky, Z.-H. Liu, I. Morozov, R. Kappenberger, S. Wurmehl, B. Büchner, A. N. Yaresko, T. K. Kim, M. Hoesch *et al.*, Nat. Phys. **12**, 311 (2016).
[73] B. J. Kim, H. Jin, S. J. Moon, J.-Y. Kim, B.-G. Park, C. S. Leem, J. Yu, T. W. Noh, C. Kim, S.-J. Oh. J.-H. Park *et al.*, Phys. Rev. Lett. **101**, 076402 (2008).
[74] M. Aichhorn, S. Biermann, T. Miyake, A. Georges, and M. Imada, Phys. Rev. B **82**, 064504 (2010).
[75] Z. P. Yin, K. Haule, and G. Kotliar, Phys. Rev. B **86**, 195141 (2012).
[76] J. K. Glasbrenner, I. I. Mazin, H. O. Jeschke, P. J. Hirschfeld, R. M. Fernandes, and R. Valentí, Nat. Phys. **11**, 953 (2015).
[77] I. Leonov, S. L. Skornyakov, V. I. Anisimov, and D. Vollhardt, Phys. Rev. Lett. **115**, 106402 (2015).
[78] G.-T. Wang, Y. Qian, G. Xu, X. Dai, and Z. Fang, Phys. Rev. Lett. **104**, 047002 (2010).
[79] T. Schickling, F. Gebhard, J. Bünemann, L. Boeri, O. K. Andersen, and W. Weber, Phys. Rev. Lett. **108**, 036406 (2012).
[80] S. Margadonna, Y. Takabayashi, M. T. McDonald, K. Kasperkiewicz, Y. Mizuguchi, Y. Takano, A. N. Fitch, E. Suard, and K. Prassides, Chem. Commun. **43**, 5607 (2008).
[81] Y. Mizuguchi, F. Tomioka, S. Tsuda, T. Yamaguchi, and Y. Takano, Phys. C (Amsterdam) **469**, 1027 (2009).
[82] M. Aichhorn, L. Pourovskii, V. Vildosola, M. Ferrero, O. Parcollet, T. Miyake, A. Georges, and S. Biermann, Phys. Rev. B **80**, 085101 (2009).
[83] T. Miyake, K. Nakamura, R. Arita, and M. Imada, J. Phys. Soc. Jpn. **79**, 044705 (2010).
[84] J. P. Perdew, K. Burke, and M. Ernzerhof, Phys. Rev. Lett. **77**, 3865 (1996).
[85] A. Subedi, L. Zhang, D. J. Singh, and M. H. Du, Phys. Rev. B **78**, 134514 (2008).
[86] M. D. Watson, T. K. Kim, A. A. Haghighirad, N. R. Davies, A. McCollam, A. Narayanan, S. F. Blake, Y. L. Chen, S. G. A. J. Schofield, M. Hoesch *et al.*, Phys. Rev. B **91**, 155106 (2015).